1. Extended Data

Figure #	Figure title One sentence only	Filename This should be the name the file is saved as when it is uploaded to our system. Please include the file extension. i.e.: *Smith_ED_Fi_1.jpg*	Figure Legend If you are citing a reference for the first time in these legends, please include all new references in the Online Methods References section, and carry on the numbering from the main References section of the paper.
Extended Data Fig. 1	February and April snowfall anomalies linked to low AASIC.	Fei_ED_Fig_1.eps	The regressions of (a) February and (b) April snowfall (unit: mm water equivalent day^{-1}) upon the negative February AASIC index for 1979−2018. Those values exceeding 95% confidence interval are denoted by gridding. The brown lines mark the axes of the climatological polar and subtropical westerly jets here and hereafter. The thick black line marks the boundary of the TP, based on the altitude of 2600 m above sea level here and hereafter.
Extended Data Fig. 2	Lead-lag circulation anomalies linked to low AASIC.	Fei_ED_Fig_2.eps	The regressions of (a) January, (b) February, (c) March and (d) April Rossby wave source (shaded; unit: 10^{-10} s^{-2})/geopotential height (contours; unit: 10 m) at 200 hPa upon the negative February AASIC index for 1979−2018. Those values of Rossby wave source exceeding 95% confidence interval are denoted by gridding. The solid and dashed contours respectively indicate positive and negative values here and hereafter.
Extended	Land-atmosphe	Fei_ED_Fig_3	The correlations between 2 m air

Data Fig. 3	re coupling in February and April.	.eps	temperature and snow water equivalent in (a) February and (b) April for 1979−2018. Those values exceeding 99% confidence interval are denoted by gridding.
Extended Data Fig. 4	March snowpack anomalies linked to low AASIC.	Fei_ED_Fig_4 .eps	The regressions of March snow water equivalent (shaded; unit: cm)/2 m air temperature (contours; unit: ºC) upon the negative February AASIC index for 1979−2018. Those values of snow water equivalent exceeding 95% confidence interval are denoted by gridding.
Extended Data Fig. 5	April blocking activity anomalies linked to low AASIC and low Ural SWE.	Fei_ED_Fig_5 .eps	(a) The time evolutions of the normalized negative February AASIC (black), April TP 10 m wind speed from the ERA-Interim (blue) and negative April Ural SWE (red). The regressions of April frequency of blocking heights (shaded; unit: %)/geopotential height (contours; unit: 10 m) at 500 hPa upon (b) the negative February AASIC and (c) the negative April Ural SWE indices for 1979−2018. Those values of frequency of blocking heights exceeding 95% confidence interval are denoted by gridding. The red rectangular box marks the region used to define the Ural SWE index in (b).
Extended Data Fig. 6	February AASIC, April snowpack and circulation anomalies linked to low Ural SWE.	Fei_ED_Fig_6 .eps	The regressions of (a) February sea-ice concentration (shaded; unit: %)/surface turbulent (sensible + latent) heat flux (contours; unit: 10^5 J m^{-2}), (b) April snow water equivalent (shaded; unit: cm)/2 m air temperature (contours; unit: ºC) and (c) April zonal wind (shaded; unit: m s^{-1})/geopotential height (contours; unit: 10 m) at 200 hPa upon the negative April Ural SWE index for 1979−2018. Those values of (a) turbulent heat flux, (b) snow water equivalent and (c) zonal wind exceeding 95% confidence interval are

			denoted by gridding. The red line marks the sea-ice edge in (a).
Extended Data Fig. 7	April horizontal and vertical circulation climatology over the “Pan-Third Pole” and linked to TP 10 m wind speed.	Fei_ED_Fig_7.eps	The climatological (a) 10 m horizontal wind (vectors; unit: m s^{-1})/AOD 550 nm observed by MODIS (shaded) and (b) vertical-zonal wind (vectors; unit: m s^{-1})/vertical velocity (shaded; unit: m s^{-1}) along 28ºN in April for 2003−2018. (c, d) As (a, b) except for the regressions upon the April TP 10 m wind speed index from the ERA-Interim. Those values of (c) AOD and (d) vertical-zonal wind exceeding 99% confidence interval are denoted by gridding. The circle and square respectively mark the locations of Nam Co and QOMS in (a, c). The vertical component is multiplied by 100 in (b, d). Topography is shaded by black in (b, d). The vectors of horizontal wind and vertical-zonal wind are plotted where the scales are respectively greater than 0.75 m s^{-1} in (a)/0.15 m s^{-1} in (c) and 0.4 m s^{-1} in (d).
Extended Data Fig. 8	April backward trajectories at QOMS in 2016 and 2015	Fei_ED_Fig_8.eps	The April MODIS AOD 550 nm anomalies (shaded), compared to the climatology of 2003−2018, and 3-day backward air-mass trajectories, shown by mean backward trajectory for six clusters (color lines; 3-D view shown below) arriving at QOMS (1000 m above ground level) in (a) 2016 and (b) 2015. The numbers indicate the percentages of daily trajectories with the origins. The square marks the location of QOMS.

2. Supplementary Information:

A. Flat Files

Item	Present?	Filename This should be the name the file is saved as when it is uploaded to our system, and should include the file extension. The extension must be .pdf	A brief, numerical description of file contents. i.e.: *Supplementary Figures 1-4, Supplementary Discussion, and Supplementary Tables 1-4.*
Supplementary Information	Yes	SI_r3.pdf	Supplementary Table 1 and Supplementary Figures 1−6
Reporting Summary	No		

B. Additional Supplementary Files

Complete the Inventory below for all additional Supplementary Files that cannot be submitted as part of the Supplementary Information PDF.

- Do not list Supplementary Figures in this table.
- Where possible, include the title and description within the file itself.
- Spreadsheet-based tables and data should be combined into a workbook with multiple tabs, not submitted as individual files.
- Please note that the *ONLY* allowable types of additional Supplementary Files are:
  - Supplementary Tables
  - Supplementary Videos
  - Supplementary Audio
  - Supplementary Data
  - NMR Data
  - Cryo-EM Data
  - Co
  - Su

Type	Number If there are multiple files of the same type this should be the numerical indicator. i.e. "1" for Video 1, "2" for Video 2,	Filename This should be the name the file is saved as when it is uploaded to our system, and should include the file	Legend or Descriptive Caption Describe the contents of the file

	etc.	extension. i.e.: *Smith_ Supplementary_Video_1. mov*	
Choose an item.			
Choose an item.			
Choose an item.			
Choose an item.			
Choose an item.			
Choose an item.			

3. Source Data

Parent Figure or Table	**Filename** This should be the name the file is saved as when it is uploaded to our system, and should include the file extension. i.e.: *Smith_SourceData_Fig1.xls*, or *Smith_ Unmodified_Gels_Fig1.pdf*	**Data description** e.g.: Unprocessed Western Blots and/or gels, Statistical Source Data, etc.
Source Data Fig. 1	*Fei_SourceData_Fig1.xlsx*	Statistical Source Data
Source Data Fig. 2		
Source Data Fig. 3		
Source Data Fig. 4		
Source Data Fig. 5		
Source Data Fig. 6		
Source Data Fig. 7		
Source Data Fig. 8		
Source Data Extended Data Fig. 1		

This document is the Accepted Manuscript version of a Published Work that appeared in final form in Nature Climate Change, after peer review and technical editing by the publisher.
To access the final edited and published work see https://doi.org/10.1038/s41558-020-0881-2

Source Data Extended Data Fig. 2		
Source Data Extended Data Fig. 3		
Source Data Extended Data Fig. 4		
Source Data Extended Data Fig. 5		
Source Data Extended Data Fig. 6		
Source Data Extended Data Fig. 7		
Source Data Extended Data Fig. 8		
Source Data Extended Data Fig. 9		
Source Data Extended Data Fig. 10		

Arctic sea-ice loss intensifies aerosol transport to the Tibetan Plateau

Fei Li[1]*, Xin Wan[2]*, Huijun Wang[3, 4, 5], Yvan Joseph Orsolini[6], Zhiyuan Cong[2, 7], Yongqi Gao[8, 5], Shichang Kang[9, 7]

[1]Geophysical Institute, University of Bergen and Bjerknes Centre for Climate Research, Bergen 5007, Norway

[2]Key Laboratory of Tibetan Environment Changes and Land Surface Processes, Institute of Tibetan Plateau Research, Chinese Academy of Sciences, Beijing 100101, China

[3]Collaborative Innovation Center on Forecast and Evaluation of Meteorological Disasters/Key Laboratory of Meteorological Disaster, Ministry of Education, Nanjing University of Information Science & Technology, Nanjing 210044, China

[4]Climate Change Research Center, Chinese Academy of Sciences, Beijing 100029, China

[5]Nansen-Zhu International Research Center, Institute of Atmospheric Physics, Chinese Academy

of Sciences, Beijing 100029, China
[6]NILU−Norwegian Institute for Air Research, Kjeller 2007, Norway
[7] CAS Center for Excellence in Tibetan Plateau Earth Sciences, Chinese Academy of Sciences, Beijing 100101, China
[8]Nansen Environmental and Remote Sensing Center and Bjerknes Centre for Climate Research, Bergen 5006, Norway
[9]Key Laboratory of Cryospheric Sciences, Northwest Institute of Eco-Environment and Resources, Chinese Academy of Sciences, Lanzhou 730000, China

Correspondence to: F. Li (Fei.Li@uib.no) and X. Wan (xin.wan@itpcas.ac.cn)

The Tibetan Plateau (TP) has recently been polluted by anthropogenic emissions transported from South Asia, but the mechanisms conducive to this aerosol delivery are poorly understood. Here we show that winter loss of Arctic sea ice over the subpolar North Atlantic boosts aerosol transport toward the TP in April, when the aerosol loading is at its climatological maximum and preceding the Indian summer monsoon onset. Low sea ice in February weakens the polar jet, causing decreased Ural snowpack via reduced transport of warm, moist oceanic air into the high-latitude Eurasian interior. This diminished snowpack persists through April, reinforcing the Ural pressure ridge and East Asian trough, segments of a quasi-stationary Rossby wave train extending across Eurasia. These conditions facilitate an enhanced subtropical westerly jet at the southern edge of the TP, invigorating upslope winds that combine with mesoscale updrafts to waft emissions over the Himalayas onto the TP.

The Tibetan Plateau (TP) is known as the “Third Pole” and contains the largest land ice masses outside the polar regions (Fig. 1a)[1]. Situated at a high altitude but at low latitudes, the TP has a scarce local population and limited local emission of air pollution, but it is surrounded by large deserts, such as the Taklamakan Desert in northwest China and the Thar desert in South Asia, and by the largest and heavily populated agriculture basin, i.e., the Indo-Gangetic Plain (IGP) in South Asia. These represent large sources of natural dust or anthropogenic air pollutants from biomass burning and fossil fuel usage[2]. Previous studies demonstrated that the anthropogenic aerosols from South Asia (mainly the IGP) can reach the interior of the TP after crossing the Himalayas, albeit those studies were often based on limited, discontinuous monitoring of either aerosol optical depth (AOD)[3, 4, 5], ozone[6], black carbon[7] or organic carbon[8, 9]. Such studies also indicated that frequent aerosol pollution (e.g., biomass burning) events over the TP occurred during the pre-monsoon period and that the combination of westerlies and local mountain-valley breeze acts as a transport pathway[10, 11, 12]. The light-absorbing aerosols (e.g., black carbon, brown carbon and dust) deposited on the glacier/snow surface contribute to heat and shrink the local cryospheric system[13, 14], impacting the water supply for billions of people[15, 16]. The TP surface heating also produces an “elevated heat pump” effect, lifting up aerosols hence altering the large-scale meridional tropospheric temperature gradient and increasing the Indian monsoonal precipitation[17, 18]. Although some preferred atmospheric circulation patterns could be more conducive to aerosol transport to the TP, their characteristics and the relevant mechanisms are not well understood.

The Arctic sea-ice cover over the subpolar North Atlantic, particularly in the Greenland, Barents and Kara Seas (hereafter AASIC), rapidly decreased over the past decades[19]. The influence of AASIC loss and variability onto mid-latitude Eurasia during autumn and/or winter has been extensively investigated by observational and model studies, which demonstrated an impact on the westerly jet stream and extreme weather[20, 21, 22, 23]. However, some modelling studies disagree with the observed links, and the role of AASIC reduction in the causation of these winter circulation anomalies and cold continental surface air temperature (SAT) is still under debate[24, 25, 26].

Another mid-latitude atmospheric response to the AASIC loss is the increased frequency of severe winter haze events in Eastern China, resulting from the reduced surface northerlies and the enhanced thermal stability of the lower atmosphere[27]. However, despite a previous study identifying a springtime teleconnection between the North Atlantic and TP through the propagation of a quasi-stationary Rossby wave train across Eurasia[28], there has been little focus on the impact of AASIC change at more southern Eurasian latitudes, such as over the TP.

This study presents evidence that low sea ice (AASIC) in late winter has a great potential for modulating the spring atmospheric circulation patterns across Eurasia and cross-Himalayan aerosol transport. The results are based on synthetic analysis on multi datasets such as ground-based remote sensing of AOD (Supplementary Fig. 1) and meteorological measurements at two specific stations (Nam Co and QOMS) over the TP, global satellite observations of sea ice and atmospheric and land reanalyses.

TP aerosol loading. Here we use a decade-long record of AOD 500 nm at Nam Co (2006−2016) and QOMS (2009−2017), which are respectively located in the interior of the TP and at the southern edge of the TP, just north of the Himalayas (Fig. 1a). Despite this AOD record being discontinuous, with some missing days and months in some years (Supplementary Fig. 2), a pronounced annual peak is observed in April both at Nam Co (0.093±0.039) and QOMS (0.081±0.029; Figs. 1b and 1c: black). Early studies have shown that the annual baseline values of AOD observed at the two stations are nearly equal and very low (0.029 at Nam Co and 0.027 at QOMS)[5], which reflects the background aerosol loading. In some extreme events in April, the daily AOD at the two stations has a sharp increase by 10−20 times relative to the baseline values (Supplementary Figs. 2c and 2d), suggesting transport of exogenous aerosols from the surrounding areas (e.g., the Taklamakan Desert and the IGP).

The AOD and Ångström exponent (AE; as a qualitative indicator of aerosol particle size, with low AE indicating coarse particles) can be used together to classify aerosol types into the clean continental background, dust, anthropogenic aerosols (e.g., from biomass burning) or else aerosol mixtures, with a unique criterion over the TP

(Supplementary Fig. 3)[5]. The anthropogenic and dust aerosols are respectively fine and coarse in size[29]. Further, the spectral deconvolution algorithm was applied to separate AOD into fine- and coarse-mode AOD (Supplementary Table 1)[30]. Again, it retrieves an annual peak of fine-mode AOD in April at Nam Co (0.047±0.042) and QOMS (0.065±0.031; Figs. 1b and 1c: orange). It is also noteworthy that, in April, the fine- and coarse-mode AOD are equivalent at Nam Co, but the fine-mode AOD prevails at QOMS (Supplementary Fig. 4). The fine-mode AOD is linearly linked to the surface wind speed on the daily timescale only at QOMS, while the fine-mode AOD at QOMS and Nam Co are closely correlated (Supplementary Fig. 5). This evidence suggests that the anthropogenic emissions from South Asia can waft over the Himalayas when the wind speed is large and spread to the interior of the TP[11].

The *in situ* records of surface wind speed and precipitation (2006−2016) indicate that Nam Co and QOMS are under the same climate regime. The meteorological conditions are characterized by strong mid-latitude westerlies in winter and by heavy Indian monsoon precipitation in summer[31]. As such, Nam Co (QOMS) exhibits maximum 1.5 m (2 m) wind speed in January (February) and maximum precipitation in August (July) (Figs. 1d and 1e). Besides, in the winter and pre-monsoon season, the East Asian subtropical westerly jet (EASWJ) is found at the southern edge of the TP (at about 28ºN)[32], and the observed intensity of the westerlies is much stronger at QOMS than at Nam Co. A more detailed discussion of the transport of aerosols related to strong westerlies will be elucidated in the following section.

Arctic-Ural-TP teleconnection. Attention now turns to the potential impacts of winter AASIC change. Using a regression method, we consider how the sea-ice variability in February influences the late-winter and spring circulations across Eurasia, through modulation of the EASWJ position and intensity, blocking activity and quasi-stationary Rossby waves. Figure 2a illustrates the February sea-ice concentration and surface turbulent (sensible + latent) heat flux anomalies over the subpolar North Atlantic, regressed upon the negative February AASIC index for 1979−2018. Reduced sea-ice concentrations along the sea-ice edge concur with

This document is the Accepted Manuscript version of a Published Work that appeared in final form in Nature Climate Change, after peer review and technical editing by the publisher.
To access the final edited and published work see https://doi.org/10.1038/s41558-020-0881-2

negative turbulent heat flux anomalies, which indicate above-normal heat flux from the ocean to the atmosphere, and raised local SAT and air temperature aloft (Figs. 3a and 3b: contours). Moreover, the meridional gradient of the mean tropospheric temperature reduces at northern Eurasian latitudes, and as a result, there is a marked deceleration of 200-hPa zonal wind from the core of the polar jet over western Europe across northern Eurasia (Figs. 3b and 3c: shaded). This zonal wind decrease leads to a lessened transport of warmer, moister oceanic air, thereby reducing snowfall (Extended Data Fig. 1a) and snow water equivalent (SWE; Fig. 3a: shaded) across the 45º−70ºN latitudinal band. In addition, cold anomalies emerge particularly over central and eastern Eurasia. The gradient increases further south, across the 20º−45ºN latitudinal band, enhancing the 200-hPa zonal wind on the northern flanks of two anticyclones situated along the climatological axis of the EASWJ, and increasing SWE over the western TP.

One must assess the question of causality between the sea-ice variability in February and these circulation impacts[24, 33]. For example, pre-existing circulation anomalies might very well be the cause of the sea-ice loss as well as the cause of the aforementioned impacts. First, the turbulent heat fluxes over the sea-ice loss region are upward in February (Fig. 2a), indicating an oceanic influence upon the atmosphere. Moreover, a lead-lag correlation analysis (Extended Data Fig. 2) indeed reveals a pre-existing wave train in January that can be interpreted as quasi-stationary Rossby waves trapped along the polar jet waveguide, and excited by an anomalous upper-level Rossby wave source over the North Atlantic. The anticyclone in the Barents-Kara Seas, as part of this wave train, advects anomalously warm air poleward and promotes local sea-ice melt. Yet, the sea-ice loss reinforces the anticyclone and promotes the wave train extension further eastwards into Eurasia in February. The anomalous wave train does not persist to March but re-emerges in April. To understand April re-emergence, we investigate the coupling with land surface processes.

The snowpack on land is a slowly evolving component of the climate system, intimately involved in the land-atmosphere coupling. The local coupling between

SWE and the overlying SAT, calculated as their monthly-mean correlation (Extended Data Fig. 3), is largely negative over mid-latitude Eurasia in winter and over high-latitude Eurasia in spring. In winter, SWE is effectively decoupled from SAT over high-latitude Eurasia due to the persistently thick snowpack[34, 35]. The regressed negative SWE anomalies over mid-latitude Eurasia in February are maintained and even strengthen in March (Extended Data Fig. 4). In April, they become increasingly pronounced over the Ural region, coinciding with raised local SAT (Fig. 4a). Also, over the Ural region, there is an anomalously reinforced, warm-core pressure ridge at 200 hPa (Figs. 4b and 4c: contours). This evidence is suggestive of positive feedback by which the reduced SWE and warm anomalies help increase the frequency of Ural blockings by enhancing anomalous baroclinicity on their northern flank (Fig. 4b and Extended Data Fig. 5)[36]; on the other hand, the presence of Ural pressure ridge hinders the extension of the polar jet over Europe and favours reduced snowpack (Extended Data Figs. 1b). Furthermore, there is a quasi-stationary Rossby wave train across Eurasia, which consists of an enhanced Ural pressure ridge and a deepened East Asian trough further east. A pronounced acceleration of 200-hPa zonal wind emerges along the southern flank of the East Asian trough, which is indicative of a stronger EASWJ (Fig. 4c).

Thus, the results confirm a spring (April) “Arctic-Ural-TP” teleconnection[28], and the variability of February AASIC is a key driver of circulation anomalies particularly over the “Pan-Third Pole”, referred as the Euro-Asian highlands and their surroundings[37], modulating the intensity of EASWJ. It is also noteworthy that the variability of April Ural SWE is closely correlated with that of February AASIC (Extended Data Fig. 5a). The circulation anomalies related to low AASIC are well represented by regressions onto a low Ural SWE index (Extended Data Fig. 6). It further confirms that the land surface processes over the Ural region (namely the snowpack) play a key role in conveying the memory of the AASIC impacts into the spring months[38].

Aerosol delivery to the TP. We further explore the link between AASIC and 10 m wind speed over the TP established by the aforementioned teleconnection. To this end, we computed the lead-lag correlations of the month-to-month AASIC with April TP 10 m wind speed for 1979−2018. The latter was derived from two datasets: first, from the weighted average of *in situ* observations at the 66 TP stations and, secondly, from collocated reanalysis from the ERA-Interim. The April TP 10 m wind speed from *in situ* and reanalysis data are significantly correlated, and both are linear related to February AASIC (Supplementary Fig. 6). The time series of February AASIC and April TP 10 m wind speed from the ERA-Interim are shown in Figure 2d.

Shifting focus to the "Pan-Third Pole", the climatological distributions of satellite-derived AOD at 550 nm/10 m horizontal wind and vertical-zonal wind along 28ºN in April for 2003−2018 are respectively shown in Extended Data Figures 7a and 7b. In April, two major source regions of the aerosols that directly influence the TP can be identified as the Taklamakan Desert and the IGP, respectively to the north and the south of the TP[2]. The prevailing surface winds are westerlies along the southern flank of the Euro-Asian highlands and over the high-altitude TP, and northwesterly winds in the IGP. The vertical-zonal cross-section along 28ºN exhibits strong westerlies in the upper troposphere and ascent on the windward slopes of the Iranian Plateau and TP. The argument for how the low AASIC can modulate the aerosol transport is illustrated in Figures 5a and 5b, which shows the corresponding regression analysis based on the negative February AASIC index. The IGP and the southern TP are respectively under the influence of strong surface northwesterly and westerly anomalies, accompanied by anomalous upslope winds over the Himalayas. Meanwhile, MODIS observations reveal an accumulation of elevated AOD values at the southern edge of the TP (Fig. 5a: shaded).

We surmise that, first, the low AASIC-related, enhanced surface northwesterly winds in the IGP are possibly relevant in accounting for the accumulation of aerosols at the southern edge of the TP. Second, the low AASIC could strengthen the EASWJ which extends westward toward the IGP and leads to surface northwesterly anomalies in the IGP and anomalous upslope winds over the Himalayas presumably due to an interaction of the flow with the topography (Figs. 5b and Extended Data Fig. 7d)[32].

Taken together, it would be conducive to synoptic-scale or mesoscale processes that carry the polluted air masses, mostly originating from the IGP, wafting over the Himalayas and reaching the interior of the TP[11]. The same regressions but using the April TP 10 m wind speed index from the ERA-Interim supports that hypothesis, elucidating the role of strong surface westerlies over the TP (Extended Data Figs. 7c and 7d).

A better understanding of the transboundary transport of aerosols to the TP in relation to the low sea ice (AASIC) can be obtained by contrasting the two months of April 2016 and 2015, which respectively occurred during low and high AASIC years, in terms of AOD as observed by MODIS and of 3-day backward air-mass trajectories arriving at QOMS (Extended Data Fig. 8)[6]. The low-level trajectories (e.g., at heights below 4 km before their ascent over the Himalayas) are the most relevant to interpret the observed aerosol accumulation at QOMS. First, in 2016, due to surface northwesterly anomalies in the IGP combined with a stronger EASWJ, the air masses that arrived at QOMS were predominantly from the west, with the most abundant 3-D clusters representing 39.5% of trajectories at the lower levels and 20% at the upper levels. Air parcels belonging to the low-level cluster traversed a moderately polluted IGP before encountering a heavily polluted region at the southern edge of the TP as they moved upslope over the Himalayas. In comparison, in 2015, the two more abundant clusters were from the south and at the lower levels (44.7% and 25.7%), which indicate that the air masses travelled relatively slowly, originating closer to the TP and arriving at QOMS after traversing lowly polluted southern slopes of the Himalayas. Hence, larger values of fine-mode AOD were retrieved at QOMS in April 2016, compared to April 2015 (Fig. 2c), despite central India and the Arabian Sea having overall higher AOD values according to MODIS in 2015 than in 2016. The more intense low-level winds across the IGP in 2016 seemed to be important in blowing polluted air eastwards, accumulating the pollutants on the southern fringes of the Himalayas, as is also characteristics of April months in low sea-ice years (see Fig. 5a).

The trajectory analysis above highlights the importance of sustained surface winds. The regression maps of February sea-ice concentration, April SWE and April 200-hPa geopotential height onto the April TP 10 m wind speed index from ERA-Interim (Fig. 5c) also identifies an "Arctic-Ural-TP" teleconnection, involving a reinforced Ural pressure ridge and a deepened East Asian trough at 200 hPa. All of these are broadly similar to the corresponding AASIC-regressed fields (Figs. 2a, 4a and 4c).

Discussion

The largest aerosol loading over the TP emerges in April, preceding the Indian summer monsoon onset, a period when there are extensive forest fire and agriculture residue burning emissions in South Asia (mainly in the IGP)[9, 39]. This study demonstrates that there is a connection between the delivery of the atmospheric pollutants from South Asia to the TP in April and the variability of February AASIC. We also emphasize the important linking role of the slowly evolving snowpack over the Ural region. When a below-normal SWE persists to April, as caused by the low sea ice in February weakening the polar jet, the Ural pressure ridge/East Asian trough dipole that is part of a slowly propagating Rossby wave train along the polar jet get reinforced. As a result, an intensified EASWJ is found at the southern edge of the TP, which eventually strengthens upslope winds wafting up aerosols over the Himalayas and inwards onto the TP.

It is not yet clear how much of aerosol loading could reach the TP in response to AASIC decrease on the multi-annual and longer timescales. A principal obstacle to quantitative analysis is the lack of sufficient *in situ* measurements of aerosols over the TP and the "Pan-Third Pole", at high spatial and temporal resolution[2, 10]. Monitoring of the aerosol loading over the TP has only been started in the recent decade. Future studies should also include tracer transport modelling, a task that is beyond the scope of the present investigation.

This study offers new perspectives on understanding the aerosol loading over the TP. Local measurements cannot be understood in isolation, primarily because climate change also affects the aerosol long-range transport to the TP. In the context of global warming, winters with low AASIC, conducive to the accumulation of aerosols over the TP, are more likely to be more common (see Fig. 2). Potential consequences might include the demise of Tibetan glaciers[13, 14], as well as the deleterious effect of glacier loss on freshwater supplies, a serious environmental risk. It is noteworthy that the TP warming rate is more than two times the global warming rate over the past three decades[10, 15]. Therefore, the reduction of anthropogenic emissions is the only way that might curb this environmental risk.

References

1. Yao T, Thompson LG, Mosbrugger V, Zhang F, Ma Y, Luo T*, et al.* Third Pole Environment (TPE). *Environmental Development* 2012, **3:** 52-64.

2. Qiu J. China: The third pole. *Nature* 2008, **454**(7203)**:** 393-396.

3. Xia XG, Zong XM, Cong ZY, Chen HB, Kang SC, Wang PC. Baseline continental aerosol over the central Tibetan plateau and a case study of aerosol transport from South Asia. *Atmos Environ* 2011, **45**(39)**:** 7370-7378.

4. Zhu J, Xia X, Che H, Wang J, Cong Z, Zhao T*, et al.* Spatiotemporal variation of aerosol and potential long-range transport impact over Tibetan Plateau, China. *Atmos Chem Phys* 2019**:** 1-34.

5. Pokharel M, Guang J, Liu B, Kang S, Ma Y, Holben BN*, et al.* Aerosol properties over Tibetan Plateau from a decade of AERONET measurements: baseline, types, and influencing factors. *Journal of Geophysical Research: Atmospheres* 2019.

6. Yin X, Kang S, de Foy B, Cong Z, Luo J, Zhang L*, et al.* Surface ozone at Nam Co in the inland Tibetan Plateau: variation, synthesis comparison and regional representativeness. *Atmos Chem Phys* 2017, **17**(18)**:** 11293-11311.

7. Chen X, Kang S, Cong Z, Yang J, Ma Y. Concentration, temporal variation, and sources of black carbon in the Mt. Everest region retrieved by real-time observation and simulation. *Atmos Chem Phys* 2018, **18**(17)**:** 12859-12875.

8. Wan X, Kang S, Wang Y, Xin J, Liu B, Guo Y*, et al.* Size distribution of carbonaceous aerosols at a high-altitude site on the central Tibetan Plateau (Nam Co Station, 4730ma.s.l.). *Atmospheric Research* 2015, **153:** 155-164.

9. Cong Z, Kang S, Kawamura K, Liu B, Wan X, Wang Z*, et al.* Carbonaceous aerosols on the south edge of the Tibetan Plateau: concentrations, seasonality and sources. *Atmos Chem Phys* 2015, **15**(3)**:** 1573-1584.

10. Kang S, Zhang Q, Qian Y, Ji Z, Li C, Cong Z*, et al.* Linking atmospheric pollution to cryospheric change in the Third Pole region: current progress and future prospects. *National Science Review* 2019.

11. Lüthi ZL, Škerlak B, Kim SW, Lauer A, Mues A, Rupakheti M*, et al.* Atmospheric brown clouds reach the Tibetan Plateau by crossing the Himalayas. *Atmos Chem Phys* 2015, **15**(11)**:** 6007-6021.

12. Cong Z, Kawamura K, Kang SC, Fu PQ. Penetration of biomass-burning emissions from South Asia through the Himalayas: new insights from atmospheric organic acids. *Sci Rep-Uk* 2015, **5**.

13. Xu B, Cao J, Hansen J, Yao T, Joswia DR, Wang N*, et al.* Black soot and the survival of Tibetan glaciers. *Proc Natl Acad Sci U S A* 2009, **106**(52)**:** 22114-22118.

14. Li C, Bosch C, Kang S, Andersson A, Chen P, Zhang Q*, et al.* Sources of black carbon to the Himalayan-Tibetan Plateau glaciers. *Nat Commun* 2016, **7:** 12574.

15. Yao T, Xue Y, Chen D, Chen F, Thompson L, Cui P*, et al.* Recent Third Pole's Rapid Warming Accompanies Cryospheric Melt and Water Cycle Intensification and Interactions between Monsoon and Environment: Multidisciplinary Approach with Observations, Modeling, and Analysis. *Bulletin of the American Meteorological Society* 2019, **100**(3)**:** 423-444.

16. Immerzeel WW, van Beek LP, Bierkens MF. Climate change will affect the Asian water towers. *Science* 2010, **328**(5984)**:** 1382-1385.

17. Senan R, Orsolini YJ, Weisheimer A, Vitart F, Balsamo G, Stockdale TN*, et al.* Impact of springtime Himalayan–Tibetan Plateau snowpack on the onset of the Indian summer monsoon in coupled seasonal forecasts. *Climate Dynamics* 2016, **47**(9-10)**:** 2709-2725.

18. Lau KM, Kim KM. Observational relationships between aerosol and Asian monsoon rainfall, and circulation. *Geophys Res Lett* 2006, **33**(21).

19. Stroeve JC, Kattsov V, Barrett A, Serreze M, Pavlova T, Holland M*, et al.* Trends in Arctic sea ice extent from CMIP5, CMIP3 and observations. *Geophys Res Lett* 2012, **39**.

20. Liu J, Curry JA, Wang H, Song M, Horton RM. Impact of declining Arctic sea ice on winter snowfall. *Proc Natl Acad Sci U S A* 2012, **109**(11)**:** 4074-4079.

21. Li F, Wang HJ. Autumn Sea Ice Cover, Winter Northern Hemisphere Annular Mode, and Winter Precipitation in Eurasia. *J Climate* 2013, **26**(11)**:** 3968-3981.

22. Gao YQ, Sun JQ, Li F, He SP, Sandven S, Yan Q*, et al.* Arctic Sea Ice and Eurasian Climate: A Review. *Adv Atmos Sci* 2015, **32**(1)**:** 92-114.

23. Vihma T. Effects of Arctic Sea Ice Decline on Weather and Climate: A Review. *Surv Geophys* 2014, **35**(5)**:** 1175-1214.

24. Screen JA, Deser C, Smith DM, Zhang X, Blackport R, Kushner PJ*, et al.* Consistency and discrepancy in the atmospheric response to Arctic sea-ice loss across climate models. *Nat Geosci* 2018, **11**(3)**:** 155-163.

25. Cohen J, Zhang X, Francis J, Jung T, Kwok R, Overland J*, et al.* Divergent consensuses on Arctic amplification influence on midlatitude severe winter weather. *Nat Clim Change* 2019, **10**(1)**:** 20-29.

26. Li F, Orsolini YJ, Wang HJ, Gao YQ, He SP. Atlantic Multidecadal Oscillation Modulates the Impacts of Arctic Sea Ice Decline. *Geophys Res Lett* 2018, **45**(5)**:** 2497-2506.

27. Wang HJ, Chen HP, Liu JP. Arctic Sea Ice Decline Intensified Haze Pollution in Eastern China. *Atmos Ocean Sci Lett* 2015, **8**(1)**:** 1-9.

28. Li J, Yu R, Zhou T. Teleconnection between NAO and Climate Downstream of the Tibetan Plateau. *J Climate* 2008, **21**(18)**:** 4680-4690.

29. Eck TF, Holben BN, Sinyuk A, Pinker RT, Goloub P, Chen H*, et al.* Climatological aspects of the optical properties of fine/coarse mode aerosol mixtures. *Journal of Geophysical Research* 2010, **115**(D19).

30. O'Neill NT, Eck TF, Smirnov A, Holben BN, Thulasiraman S. Spectral discrimination of coarse and fine mode optical depth. *J Geophys Res-Atmos* 2003, **108**(D17).

31. Molg T, Maussion F, Scherer D. Mid-latitude westerlies as a driver of glacier variability in monsoonal High Asia. *Nat Clim Change* 2014, **4**(1)**:** 68-73.

32. Bao Y, You Q. How do westerly jet streams regulate the winter snow depth over the Tibetan Plateau? *Climate Dynamics* 2019, **53**(1-2)**:** 353-370.

33. Blackport R, Screen JA, van der Wiel K, Bintanja R. Minimal influence of reduced Arctic sea ice on coincident cold winters in mid-latitudes. *Nat Clim Change* 2019, **9**(9)**:** 697-704.

34. Dutra E, Schär C, Viterbo P, Miranda PMA. Land-atmosphere coupling associated with snow cover. *Geophys Res Lett* 2011, **38**(15).

35. Xu L, Dirmeyer P. Snow-atmosphere coupling strength in a global atmospheric model. *Geophys Res Lett* 2011, **38**(13)**:** n/a-n/a.

36. García-Herrera R, Barriopedro D. Northern Hemisphere snow cover and atmospheric blocking variability. *Journal of Geophysical Research* 2006, **111**(D21).

37. Yao T, Chen F, Cui P, Ma Y, Xu B, Zhu L*, et al.* From Tibetan Plateau to Third Pole and Pan-Third Pole. *Bulletin of the Chinese Academy of Sciences* 2017, **32**(9)**:** 924-931.

38. Nakamura T, Yamazaki K, Sato T, Ukita J. Memory effects of Eurasian land processes cause enhanced cooling in response to sea ice loss. *Nat Commun* 2019, **10**(1)**:** 5111.

39. Wan X, Kang S, Li Q, Rupakheti D, Zhang Q, Guo J*, et al.* Organic molecular tracers in the atmospheric aerosols from Lumbini, Nepal, in the northern Indo-Gangetic Plain: influence of biomass burning. *Atmos Chem Phys* 2017, **17**(14)**:** 8867-8885.

Acknowledgements

F.L was supported by Nordforsk ARCPATH (76654) and the National Natural Science Foundation of China (Grant No. 41875118). X.W. was supported by the National Natural Science Foundation of China (Grant No. 41807389) and the Strategic Priority Research Program of Chinese Academy of Sciences, Pan-Third Pole Environment Study for a Green Silk Road (Pan-TPE) (XDA20040501). Y.J.O. was supported by the Research Council of Norway (Grant No. SNOWGLACE #244166). The authors acknowledge support from the Nam Co Monitoring and Research Station for Multisphere Interactions and Qomolangma Atmospheric and Environmental Observation and Research Station, Chinese Academy of Sciences for providing the meteorological datasets.

Author contributions

F.L., X.W. and H.W conceived of the study. F.L., X.W. and Y.J.O. conducted the analysis. All authors contributed to the paper writing.

Competing interests

The authors declare no competing interests.

Correspondence and requests for materials should be addressed to F.L. and X.W.

Methods

Measurement stations. The Nam Co Monitoring and Research Station for Multisphere Interactions is situated in the interior of the TP (30.77ºN, 90.99ºE, 4730 m above sea level). Its purpose is to acquire meteorological, ecological and atmospheric measurements, and it has been operated since 2005[40]. The Nam Co region is surrounded by Nam Co Lake and the Nyainqêntanglha mountain. The Qomolangma Atmospheric and Environmental Observation and Research Station (QOMS) is located at the southern edge of the TP (28.36ºN, 86.95ºE, 4276 m above sea level) and at the toe of Mt. Everest. In 2005, it was established for continuous monitoring of the atmospheric and environmental processes in the Himalayas by using a solar-electricity system[41]. Glaciers and high mountains are close to this region. Under the influence of a harsh natural environment, both Nam Co and QOMS is far from human activities, with scarcely atmospheric pollutant emission. The two stations have been considered as clean background sites.

***In situ* data.** The ground-based remote sensing of spectral AOD at Nam Co (2006−2016) and QOMS (2009−2017) is provided by the AERONET (AErosol RObotic NETwork) from CIMEL Sun photometer (CE 318)[42]. CE 318 measures sun and sky luminance directly in 8 filters over visible to near-infrared wavelengths with a 1.28 full field of view every 15 minutes. The filters are at the wavelengths of 340, 380, 440, 500, 675, 870, 940, and 1020 nm, which needs 8 seconds to finish scanning. The obtained spectral radiances are used to retrieval AOD based on Beer Law and other parameters. This approximately decade-long data record has been pre- and post-calibrated, automatically cloud screened[42] and manually inspected. The accuracy of AOD was estimated to be 0.01–0.02. For the detailed instrumentation, calibration and data processing, they are discussed elsewhere[42]. The AE was determined from the wavelength dependence of AOD between 440 and 870 nm[29].

We utilized the *in situ* records (2006−2016) of daily wind speed at Nam Co (at 1.5 m) and QOMS (at 2 m), which are conducted using the automatic weather station system (Milos 520, Vaisala Co., Finland), and of daily precipitation at the two stations, which are measured with WMO 20 cm manual precipitation gauge[43, 44]. We also used the *in situ* observations (1979−2018) of monthly 10 m wind speed at the 66 stations at the altitudes of more than 2600 m above sea level over the TP, provided by the National Climate Center, China Meteorological Administration.

Satellite and reanalysis data. The monthly sea-ice concentration was retrieved from the Met Office HadISST.2 (Hadley Centre sea-ice and sea surface temperature dataset; 1850−2018)[45], at 1º×1º horizontal resolution. We utilized monthly atmospheric fields, including surface sensible and latent heat flux, SAT (at 2 m), 10 m zonal and meridional wind, snowfall, zonal wind at 200 hPa, geopotential height at 200 and 500 hPa, tropospheric temperature, meridional and vertical wind, and daily geopotential height at 500 hPa from the ERA-Interim reanalysis (1979−2018)[46]. We used monthly SWE from the ERA-Interim/Land reanalysis (a version without precipitation correction; 1979−2018)[47]. The horizontal resolution of atmospheric and land reanalysis data were 1º×1º. We applied monthly level-3 dataset of MODIS (Moderate Resolution Imaging Spectrometer) Aqua (MYD08_M3 version v6.1, corrected; 2003−2018)[48], to characterize atmospheric column AOD at 550 nm, at 1º×1º horizontal resolution.

Climatic indices. The AASIC index was defined based on the area-weighted average of sea-ice concentration along the sea-ice edge over the subpolar North Atlantic (72º−85ºN, 20ºW−90ºE). It is a region where sea-ice reductions are understood to be especially effective at influencing the atmospheric circulations in the simultaneous and subsequent months[26]. The April TP 10 m wind speed indices stemmed from the weighted average over the 66 TP stations of the *in situ* data, and from the corresponding collocated average over (26°N–40°N, 74°E–104°E) of the ERA-Interim reanalysis data. The statistically significant correlation between the two indices indicated that the atmospheric reanalysis data has some realistic degree of skill at reproducing interannual variability of the TP surface wind speed. The Ural snow water equivalent (SWE) index was defined based on the area-weighted average of

SWE over the Ural region (40º−70ºN, 20º−70ºE).

Methods. Regressions were computed over the satellite era (1979−2018), and also for 2003−2018 due to the short-term MODIS AOD dataset. To emphasize the inter-annual variability, the long-term trend has been removed prior to correlation and regression analysis from all the fields and indices. The statistical significance was assessed using a two-tailed Student's *t*-test. Blocking high events were defined as intervals in which daily 500-hPa height exceeds one standard deviation above the monthly mean for each grid cell over five consecutive days[20]. The local frequency of blocking was measured as the ratio between the number of blocked days and the total number of days. The Rossby wave source was defined as $-v_\chi \cdot \nabla\zeta$; that is, $-\nabla \cdot v_\chi (\zeta + f)$[49]. Here, v_χ is the divergence wind component, ζ is the absolute vorticity, and f is the Coriolis parameter. The sea-ice edge is the climatological contour of 15% sea-ice concentration. The axes of the polar and subtropical westerly jets are the maximum of 200-hPa westerlies over mid-high latitudes.

In order to investigate the origins and transport pathway of air masses arriving at QOMS, 3-day backward trajectories starting at 1000 m above ground level were calculated using the HYSPLIT (HYbrid Single-Particle Lagrangian Integrated Trajectory) model[50] via TrajStat in MeteoInfo (http://www.meteothink.org/). The gridded meteorological data used for the model were obtained from the Global Data Assimilation System operated by NOAA with a horizontal resolution of 1º×1º and 23 vertical levels from 1000 to 20 hPa (https://ready.arl.noaa.gov/gdas1.php). For each backward trajectory, the total run times were 72 hours with time intervals of 1 hour during the whole measurement period.

Data availability

The *in situ* meteorological data at Nam Co and QOMS[43, 44] are available from the Institute of TP Research on reasonable request. The *in situ* meteorological data at the 66 TP stations are available from the National Climate Center, China Meteorological Administration on reasonable request. The ERA-Interim/Land reanalysis data (a version without precipitation correction)[47] is available from ECMWF on request. The following publicly available data sources were used in this study:

AERONET[42]: https://aeronet.gsfc.nasa.gov.

HadISST[45]: https://www.metoffice.gov.uk/hadobs/hadisst2.

ERA-Interim[46]: https://www.ecmwf.int/en/forecasts/datasets/reanalysis-datasets/era-interim.

MODIS Aqua[48]: https://giovanni.gsfc.nasa.gov/giovanni.

Code availability

All graphics were produced using NCAR Command Language version 6.40 (https://www.earthsystemgrid.org/dataset/ncl.640.html). Scripts are available at Zenodo under the identifier https://doi.org/10.5281/zenodo.3934144.

References

40. Cong Z, Kang S, Smirnov A, Holben B. Aerosol optical properties at Nam Co, a remote site in central Tibetan Plateau. *Atmospheric Research* 2009, **92**(1)**:** 42-48.

41. Ma Y, Ma W, Zhong L, Hu Z, Li M, Zhu Z*, et al.* Monitoring and Modeling the Tibetan Plateau's climate system and its impact on East Asia. *Sci Rep* 2017, **7:** 44574.

42. Giles DM, Sinyuk A, Sorokin MG, Schafer JS, Smirnov A, Slutsker I*, et al.* Advancements in the Aerosol Robotic Network (AERONET) Version 3 database – automated near-real-time quality control algorithm with improved cloud screening for Sun photometer aerosol optical depth (AOD) measurements. *Atmospheric Measurement Techniques* 2019, **12**(1)**:** 169-209.

43. Wang Y, Wu G. Meteorological observation data from the integrated observation and research station of multiple spheres in Namco (2005-2016). National Tibetan Plateau Data Center 2018.

44. Ma Y. Meteorological observation data from Qomolangma station for atmospheric and environmental observation and research (2005-2016). National Tibetan Plateau Data Center 2018.

45. Titchner HA, Rayner NA. The Met Office Hadley Centre sea ice and sea surface temperature data set, version 2: 1. Sea ice concentrations. *Journal of Geophysical Research: Atmospheres* 2014, **119**(6)**:** 2864-2889.

46. Dee DP, Uppala SM, Simmons AJ, Berrisford P, Poli P, Kobayashi S*, et al.* The ERA-Interim reanalysis: configuration and performance of the data assimilation system. *Quarterly Journal of the Royal Meteorological Society* 2011, **137**(656)**:** 553-597.

47. Balsamo G, Albergel C, Beljaars A, Boussetta S, Brun E, Cloke H*, et al.* ERA-Interim/Land: a global land surface reanalysis data set. *Hydrology and Earth System Sciences* 2015, **19**(1)**:** 389-407.

48. Remer LA, Kaufman YJ, Tanré D, Mattoo S, Chu DA, Martins JV*, et al.* The MODIS Aerosol Algorithm, Products, and Validation. *J Atmos Sci* 2005, **62**(4)**:** 947-973.

49. Sardeshmukh PD, Hoskins BJ. The Generation of Global Rotational Flow by Steady Idealized Tropical Divergence. *J Atmos Sci* 1988, **45**(7)**:** 1228-1251.

50. Stein AF, Draxler RR, Rolph GD, Stunder BJB, Cohen MD, Ngan F. NOAA's HYSPLIT Atmospheric Transport and Dispersion Modeling System. *Bulletin of the American Meteorological Society* 2015, **96**(12)**:** 2059-2077.

Figure 1 | Aerosol and meteorological climatology at Nam Co and QOMS. (a) The elevation map of the "Pan-Third Pole", including the TP, Pamir, Hindu Kush, Tianshan, Iranian Plateau, Caucasus and Carpathians, and the geographical location of Nam Co and QOMS. The average annual cycles of AOD 500 nm (black) and fine-mode AOD 500 nm (orange) at (b) Nam Co and (c) QOMS. The average annual cycles of surface wind speed (blue; unit: m s^{-1}) and precipitation (red; unit: mm) at (d) Nam Co and (e) QOMS. The vertical bars indicate ±0.5 standard deviation in (b-e). The gray stripe marks the month that shows the peak AOD.

Figure 2 | February AASIC change and climatic indices. (a) The regressions of February sea-ice concentration (shaded; unit: %)/surface turbulent (sensible + latent) heat flux (contours; unit: 10^5 J m^{-2}) upon the negative February AASIC index for 1979−2018. Those values of turbulent heat flux exceeding 95% confidence interval are denoted by gridding. The solid and dashed contours respectively indicate positive and negative values here and hereafter. The red line marks the sea-ice edge. The time evolutions of April AOD 500 nm (black), fine-mode AOD 500 nm (orange) and surface wind speed (blue; unit: m s^{-1}) at (b) Nam Co and (c) QOMS. (d) The time evolutions of the normalized negative February AASIC (black) and April TP 10 m wind speed from the ERA-Interim (blue). The gray stripe marks the two years used for contrasting analysis in Extended Data Figure 10.

Figure 3 | February snowpack, temperature and circulation anomalies linked to low AASIC. The regressions of February (a) snow water equivalent (shaded; unit: cm)/2 m air temperature (contours; unit: ºC), (b) air temperature averaged between 600−200 hPa (contours; unit: ºC)/its meridional gradient (shaded; unit: 10^{-7} ºC m^{-1}) and (c) zonal wind (shaded; unit: m s^{-1})/geopotential height (contours; unit: 10 m)/Rossby wave activity flux (vectors; unit: m^2 s^{-2}) at 200 hPa upon the negative February AASIC index for 1979−2018. Those values of (a) snow water equivalent, (b) meridional temperature gradient and (c) zonal wind exceeding 95% confidence interval are denoted by gridding. The vectors of Rossby waves are plotted where the scales are greater than 0.4 m^2 s^{-2} in (c). The brown lines mark the axes of the climatological polar and subtropical westerly jets here and hereafter. The thick black line marks the boundary of the TP, based on the altitude of 2600 m above sea level here and hereafter.

Figure 4 | April snowpack, temperature and circulation anomalies linked to low AASIC. The regressions of April (a) snow water equivalent (shaded; unit: cm)/2 m air temperature (contours; unit: ºC), (b) air temperature averaged between 600−200 hPa (contours; unit: ºC)/its meridional gradient (shaded; unit: 10^{-7} ºC m^{-1}) and (c) zonal wind (shaded; unit: m s^{-1})/geopotential height (contours; unit: 10 m)/Rossby wave activity flux (vectors; unit: m^2 s^{-2}) at 200 hPa upon the negative February AASIC index for 1979−2018. Those values of (a) snow water equivalent, (b) meridional temperature gradient and (c) zonal wind exceeding 95% confidence interval are denoted by gridding. The vectors of Rossby waves are plotted where the scales are greater than 0.4 m^2 s^{-2} in (c). The rectangular box marks the "Pan-Third Pole" region.

Figure 5 | April horizontal and vertical circulation anomalies over the "Pan-Third Pole" linked to low AASIC and schematic representation of the Arctic-Ural-TP teleconnection. The regressions of April (a) 10 m horizontal wind (vectors; unit: m s^{-1}) and AOD 550 nm observed by MODIS (shaded) and (b) vertical-zonal wind (vectors; unit: m s^{-1}) and vertical velocity (shaded; unit: m s^{-1}) along 28ºN upon the negative February AASIC index for 2003−2018. The circle and square respectively mark the locations of Nam Co and QOMS in (a). The vertical component is multiplied by 100 in (b). Topography is shaded by black in (b). The vectors of horizontal wind and vertical-zonal wind are plotted where the scales are respectively greater than 0.1 m s^{-1} in (a) and 0.4 m s^{-1} in (b). (c) The regressions of February sea-ice concentration (shaded; unit: %)/April snow water equivalent (shaded; unit: cm)/April geopotential height at 200 hPa (contours; unit: 10 m) upon the April TP 10 m wind speed index from the ERA-Interim for 1979−2018. Those values of (a) AOD/(b) vertical-zonal wind and (c) geopotential height respectively exceeding 95% and 99% confidence intervals are denoted by gridding.

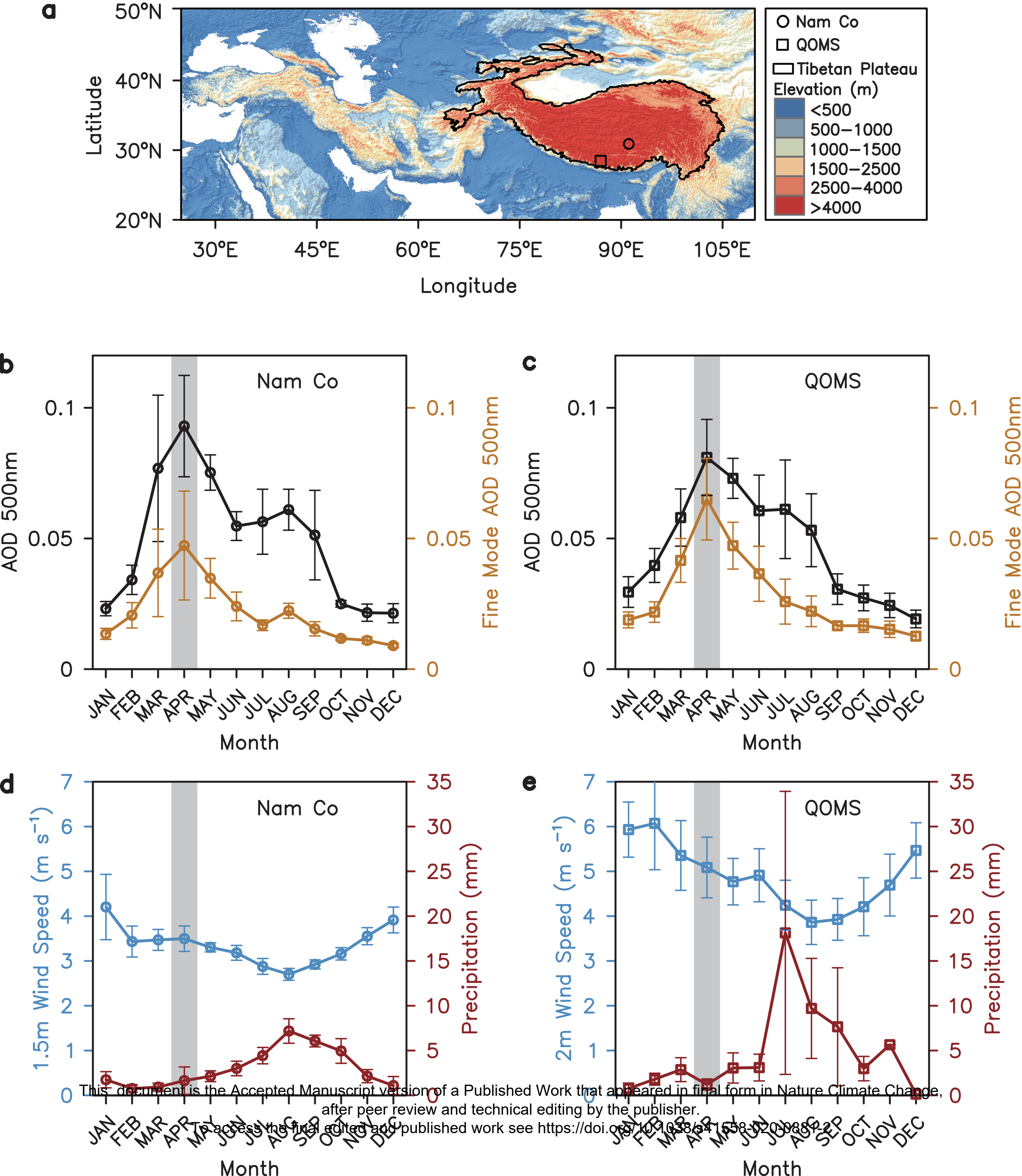
a
50°N
40°N
30°N
20°N
Latitude
30°E
45°E
60°E
75°E
90°E
105°E
Longitude
Nam Co
QOMS
Tibetan Plateau
Elevation (m)
<500
500–1000
1000–1500
1500–2500
2500–4000
>4000
b
Nam Co
AOD 500nm
Fine Mode AOD 500nm
0
0.05
0.1
JAN FEB MAR APR MAY JUN JUL AUG SEP OCT NOV DEC
Month
c
QOMS
AOD 500nm
Fine Mode AOD 500nm
0
0.05
0.1
JAN FEB MAR APR MAY JUN JUL AUG SEP OCT NOV DEC
Month
d
Nam Co
1.5m Wind Speed (m s^{-1})
Precipitation (mm)
0 1 2 3 4 5 6 7
0 5 10 15 20 25 30 35
JAN FEB MAR APR MAY JUN JUL AUG SEP OCT NOV DEC
Month
e
QOMS
2m Wind Speed (m s^{-1})
Precipitation (mm)
0 1 2 3 4 5 6 7
0 5 10 15 20 25 30 35
JAN FEB MAR APR MAY JUN JUL AUG SEP OCT NOV DEC
Month

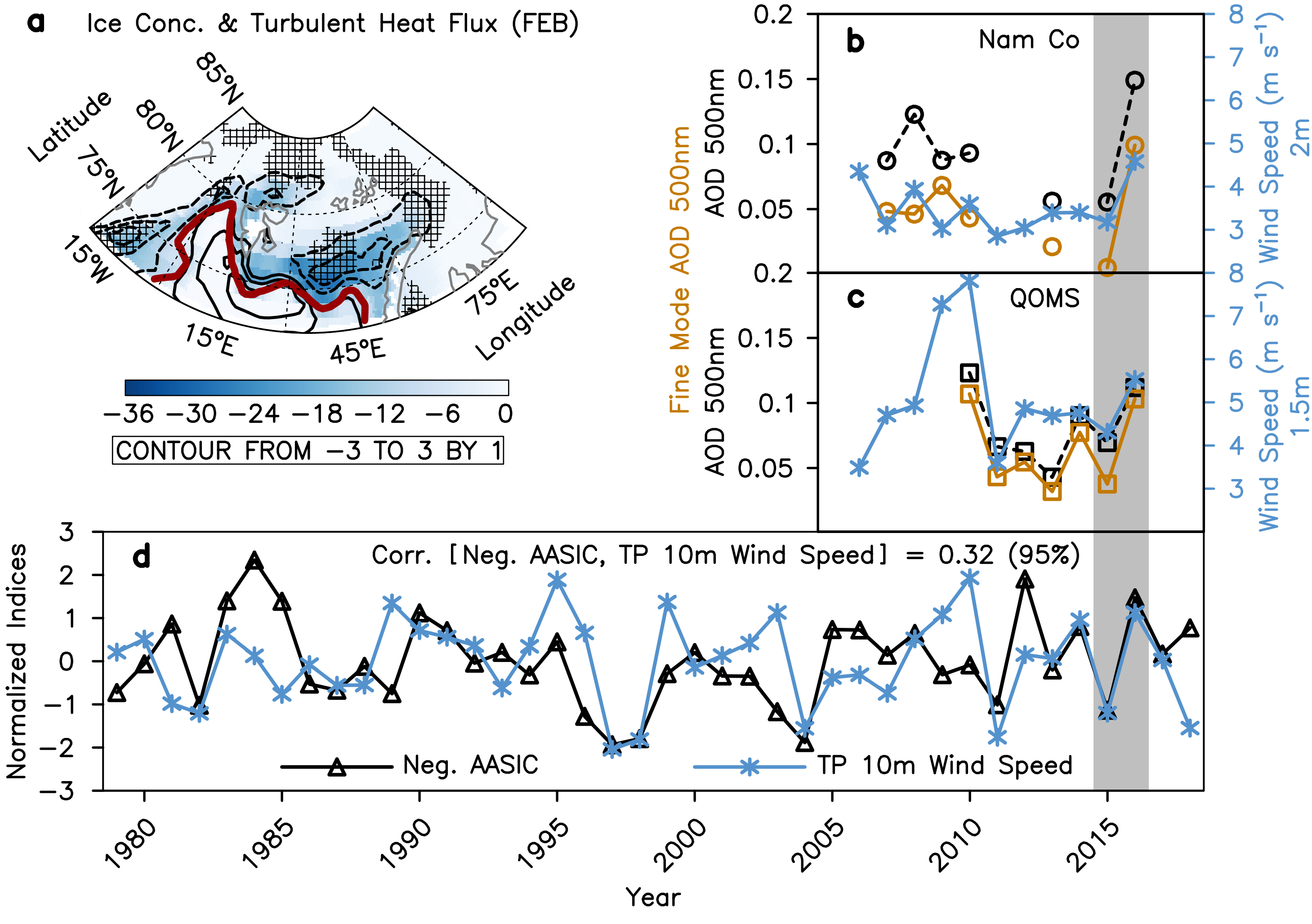

This document is the Accepted Manuscript version of a Published Work that appeared in final form in Nature Climate Change, after peer review and technical editing by the publisher.
To access the final edited and published work see https://doi.org/10.1038/s41558-020-0881-2

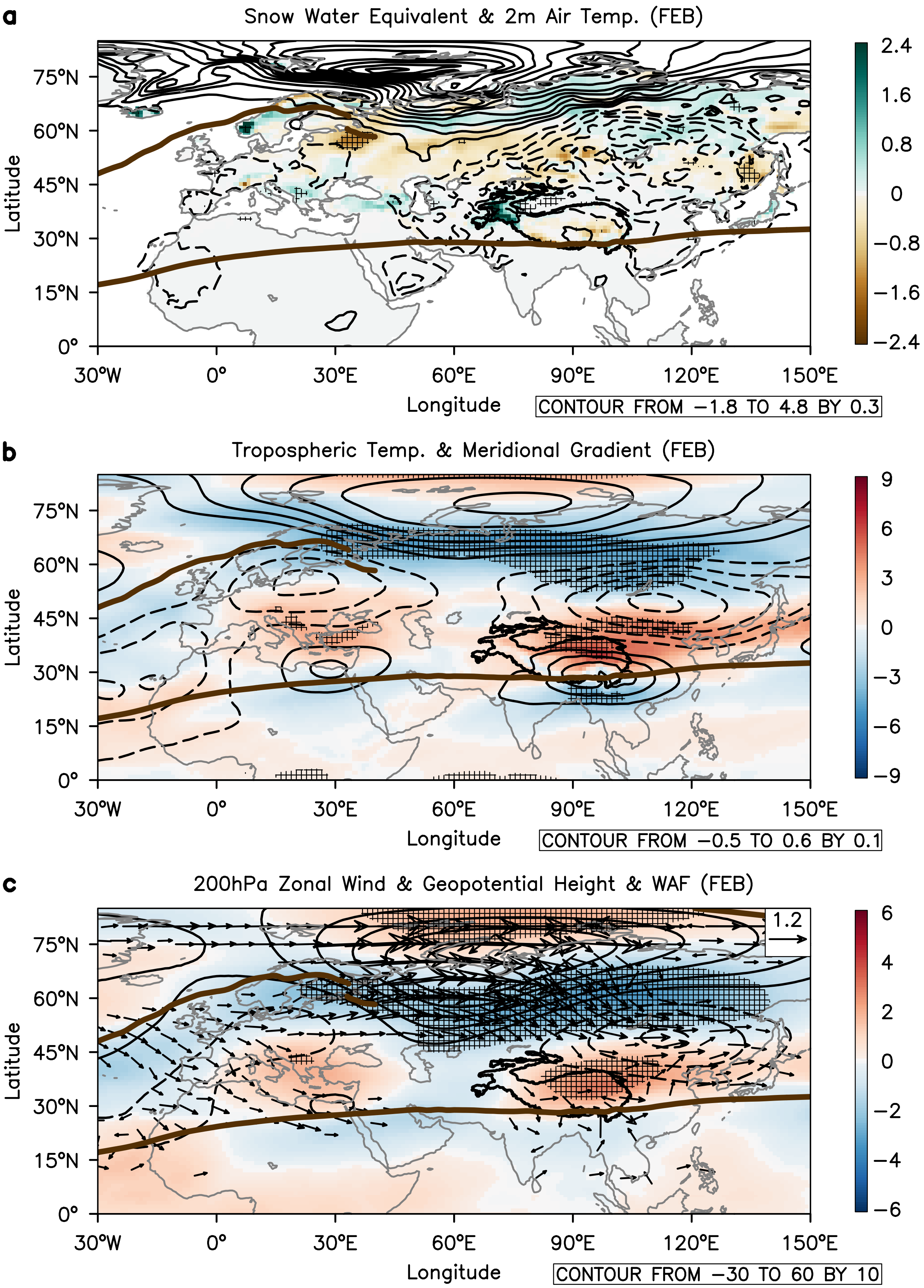
a
Snow Water Equivalent & 2m Air Temp. (FEB)
75°N
60°N
45°N
30°N
15°N
0°
Latitude
30°W
0°
30°E
60°E
90°E
120°E
150°E
Longitude
CONTOUR FROM −1.8 TO 4.8 BY 0.3
2.4
1.6
0.8
0
−0.8
−1.6
−2.4
b
Tropospheric Temp. & Meridional Gradient (FEB)
CONTOUR FROM −0.5 TO 0.6 BY 0.1
9
6
3
0
−3
−6
−9
c
200hPa Zonal Wind & Geopotential Height & WAF (FEB)
1.2
CONTOUR FROM −30 TO 60 BY 10
6
4
2
0
−2
−4
−6

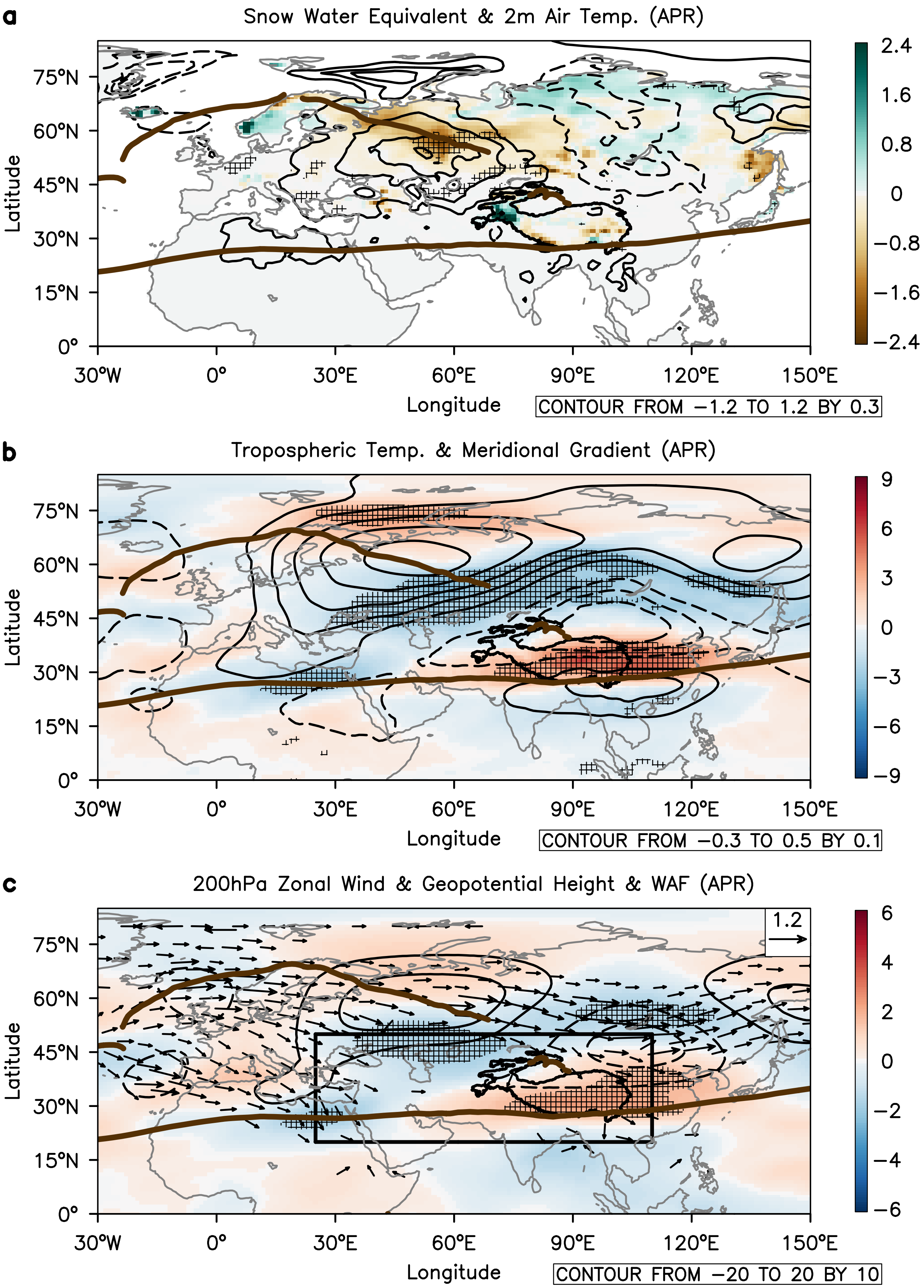
a
Snow Water Equivalent & 2m Air Temp. (APR)
75°N
60°N
45°N
30°N
15°N
0°
Latitude
30°W
0°
30°E
60°E
90°E
120°E
150°E
Longitude
CONTOUR FROM −1.2 TO 1.2 BY 0.3
2.4
1.6
0.8
0
−0.8
−1.6
−2.4
b
Tropospheric Temp. & Meridional Gradient (APR)
Latitude
Longitude
CONTOUR FROM −0.3 TO 0.5 BY 0.1
9
6
3
0
−3
−6
−9
c
200hPa Zonal Wind & Geopotential Height & WAF (APR)
1.2
Latitude
Longitude
CONTOUR FROM −20 TO 20 BY 10
6
4
2
0
−2
−4
−6

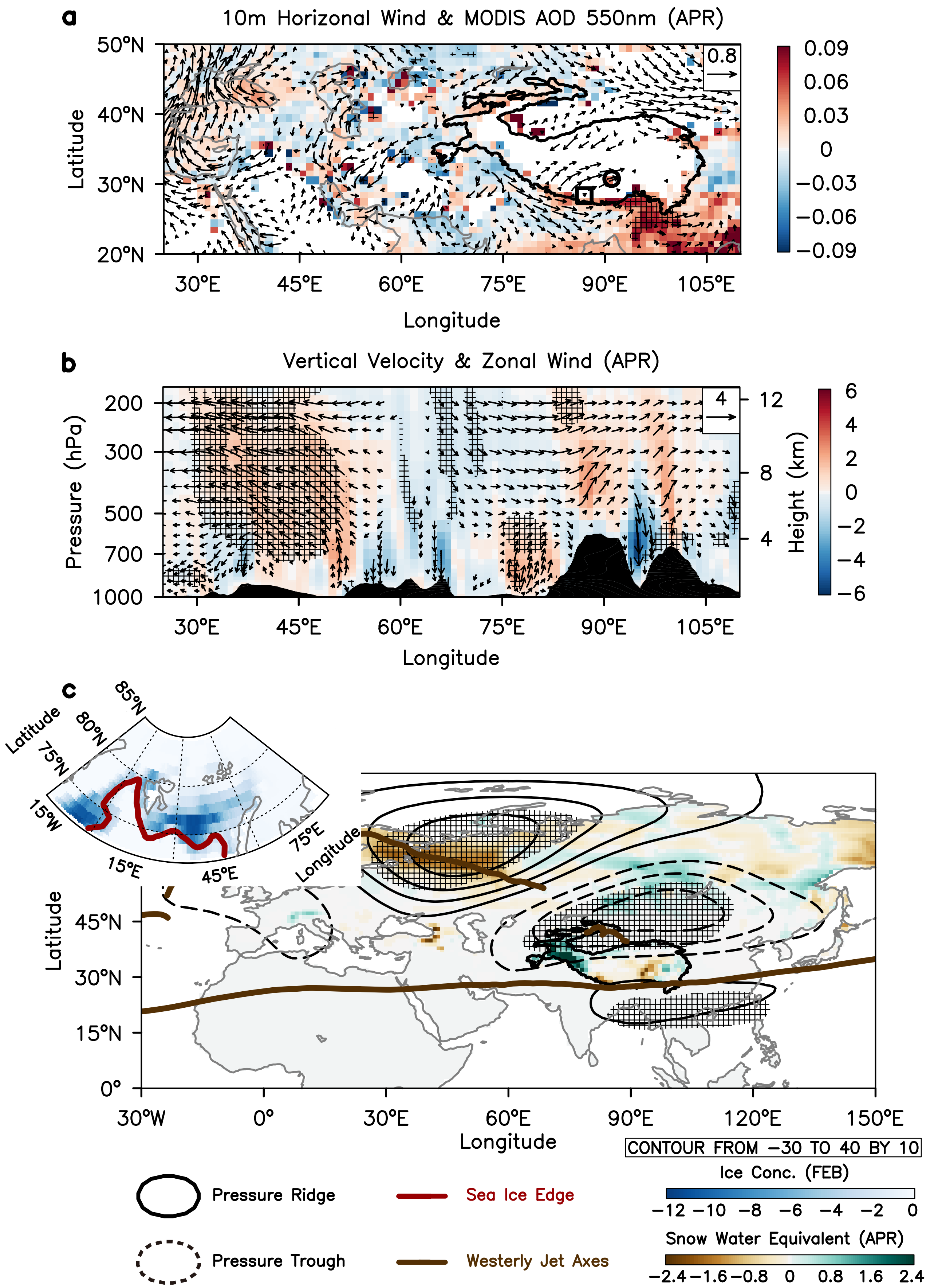
a
10m Horizontal Wind & MODIS AOD 550nm (APR)
50°N
40°N
30°N
20°N
Latitude
0.8
30°E
45°E
60°E
75°E
90°E
105°E
Longitude
0.09
0.06
0.03
0
−0.03
−0.06
−0.09
b
Vertical Velocity & Zonal Wind (APR)
200
300
500
700
1000
Pressure (hPa)
4
12
8
4
Height (km)
6
4
2
0
−2
−4
−6
30°E
45°E
60°E
75°E
90°E
105°E
Longitude
c
Latitude
85°N
80°N
75°N
15°W
15°E
45°E
75°E
Longitude
45°N
30°N
15°N
0°
Latitude
30°W
0°
30°E
60°E
90°E
120°E
150°E
Longitude
CONTOUR FROM −30 TO 40 BY 10
Pressure Ridge
Pressure Trough
Sea Ice Edge
Westerly Jet Axes
Ice Conc. (FEB)
−12 −10 −8 −6 −4 −2 0
Snow Water Equivalent (APR)
−2.4 −1.6 −0.8 0 0.8 1.6 2.4

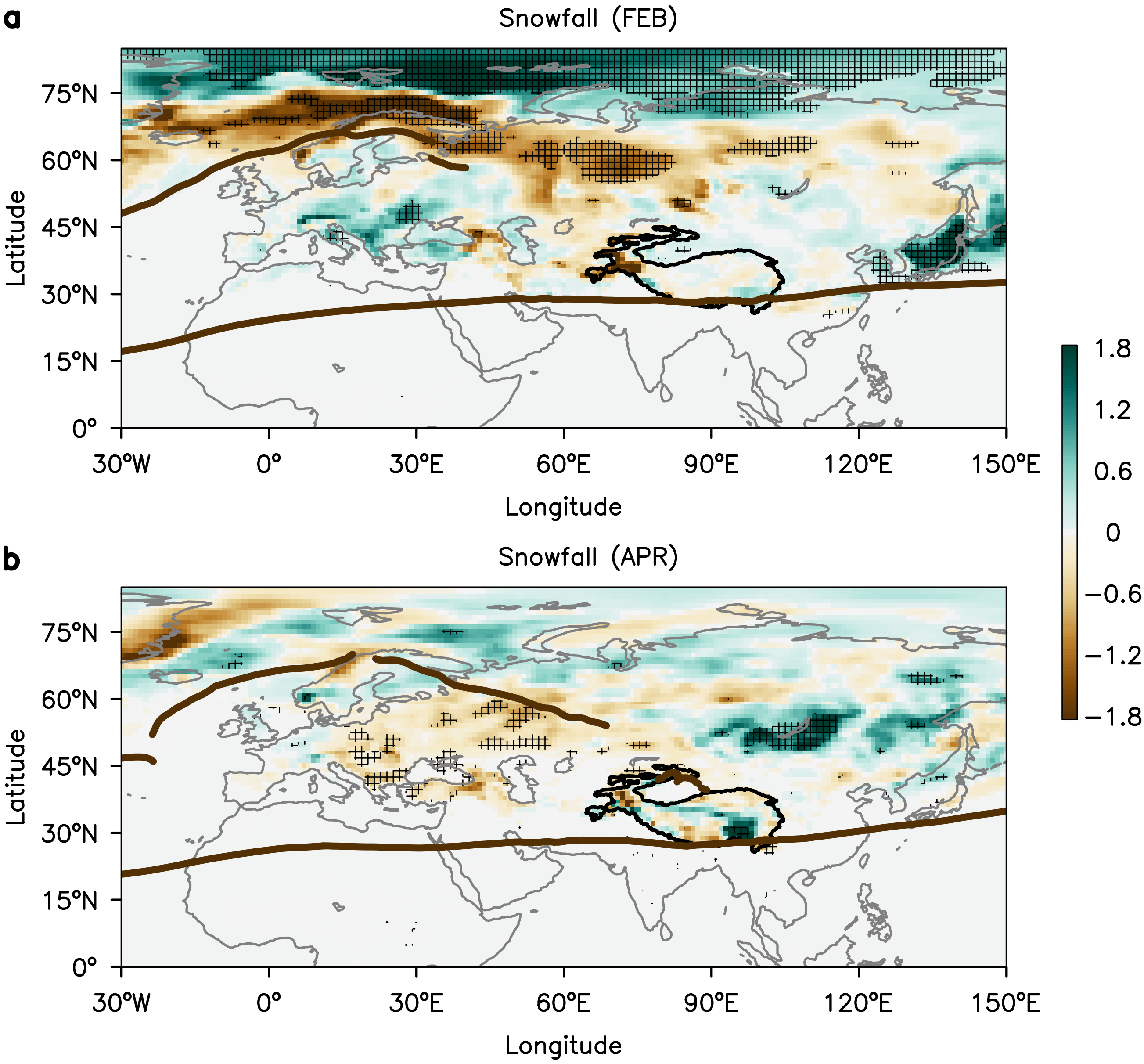
a
Snowfall (FEB)
75°N
60°N
45°N
30°N
15°N
0°
Latitude
30°W
0°
30°E
60°E
90°E
120°E
150°E
Longitude
b
Snowfall (APR)
1.8
1.2
0.6
0
−0.6
−1.2
−1.8

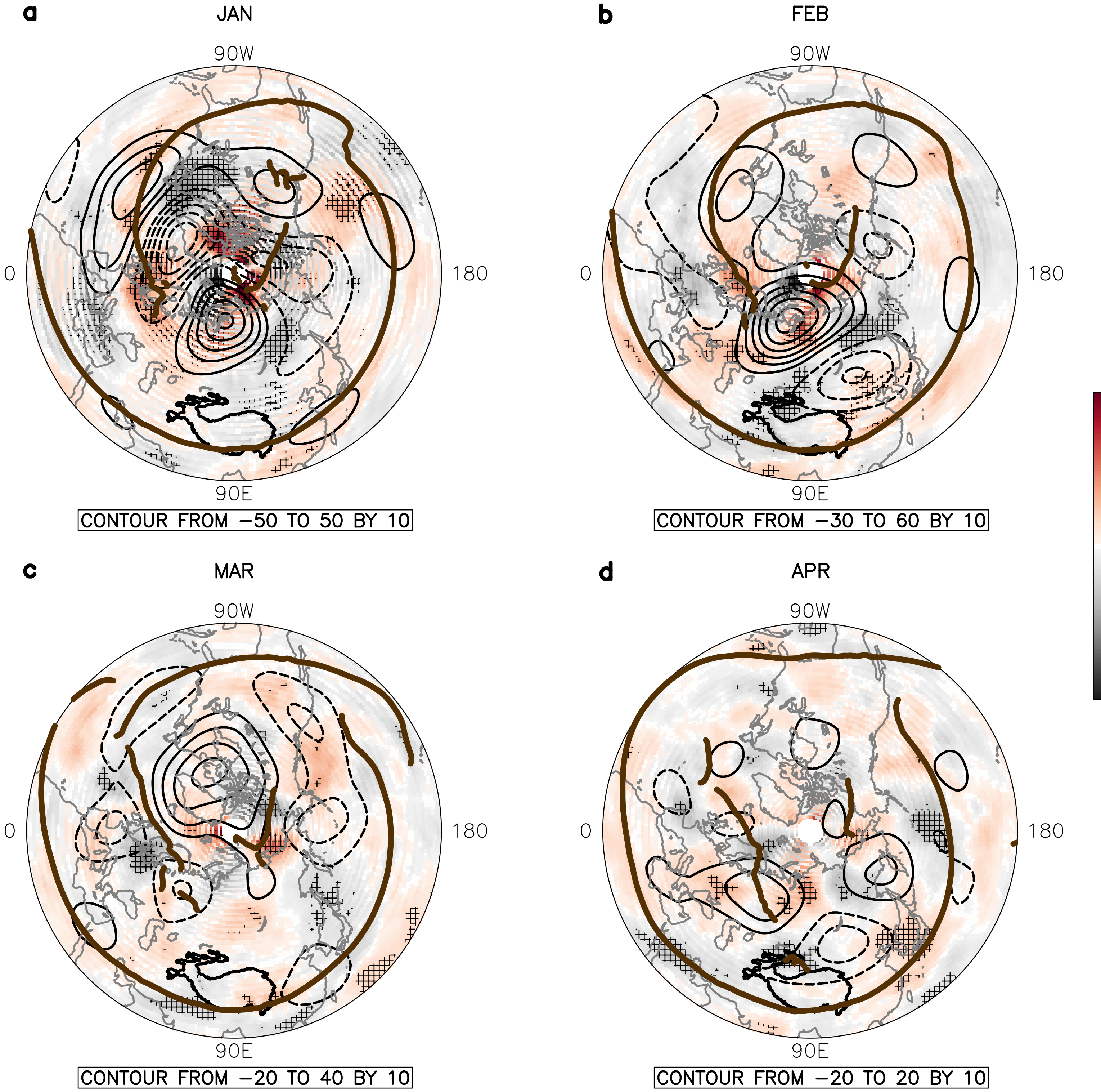
a
JAN
90W
0
180
90E
CONTOUR FROM −50 TO 50 BY 10
b
FEB
90W
0
180
90E
CONTOUR FROM −30 TO 60 BY 10
c
MAR
90W
0
180
90E
CONTOUR FROM −20 TO 40 BY 10
d
APR
90W
0
180
90E
CONTOUR FROM −20 TO 20 BY 10

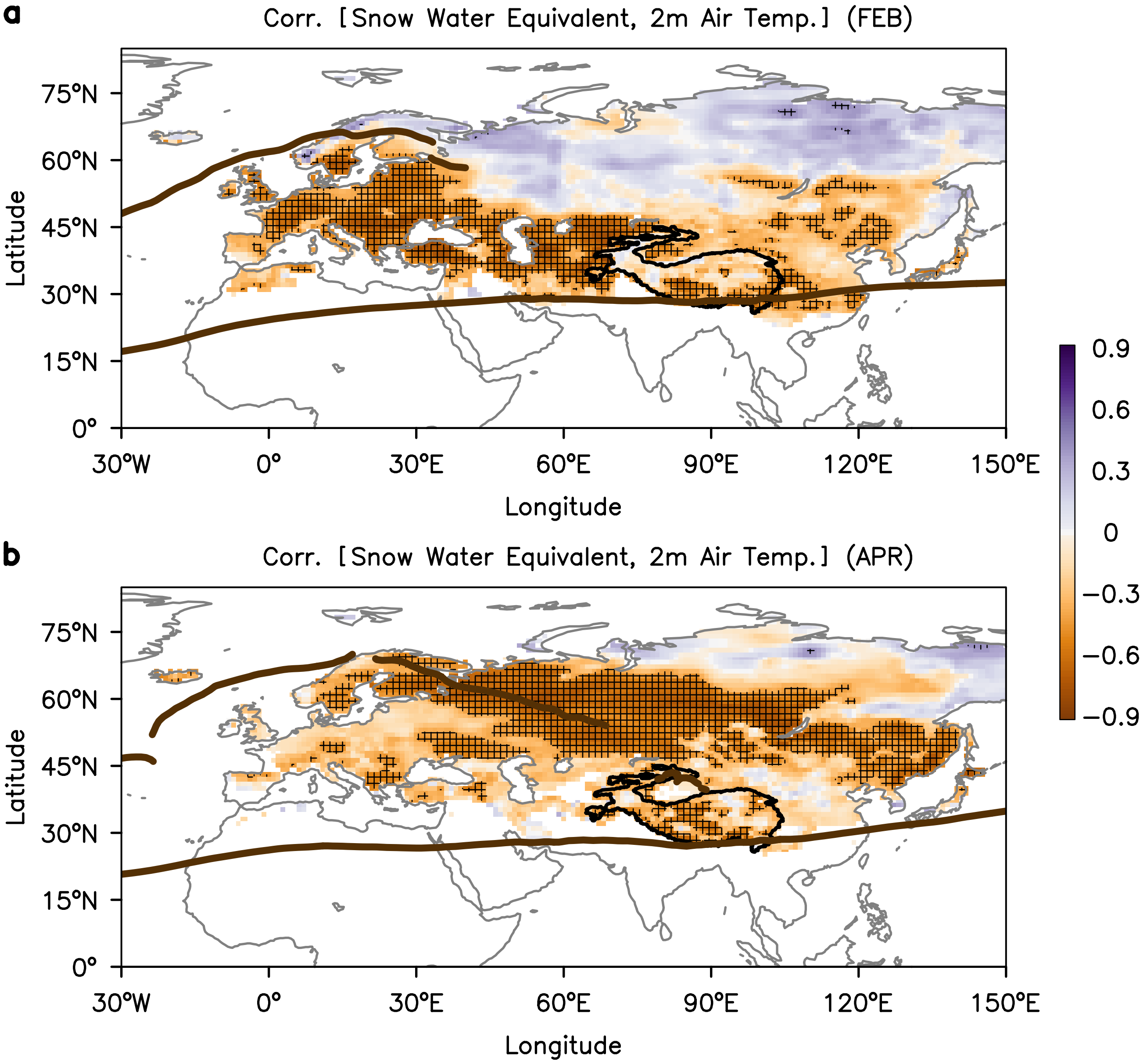
a
Corr. [Snow Water Equivalent, 2m Air Temp.] (FEB)
75°N
60°N
45°N
30°N
15°N
0°
Latitude
30°W
0°
30°E
60°E
90°E
120°E
150°E
Longitude
b
Corr. [Snow Water Equivalent, 2m Air Temp.] (APR)
75°N
60°N
45°N
30°N
15°N
0°
Latitude
30°W
0°
30°E
60°E
90°E
120°E
150°E
Longitude
0.9
0.6
0.3
0
−0.3
−0.6
−0.9

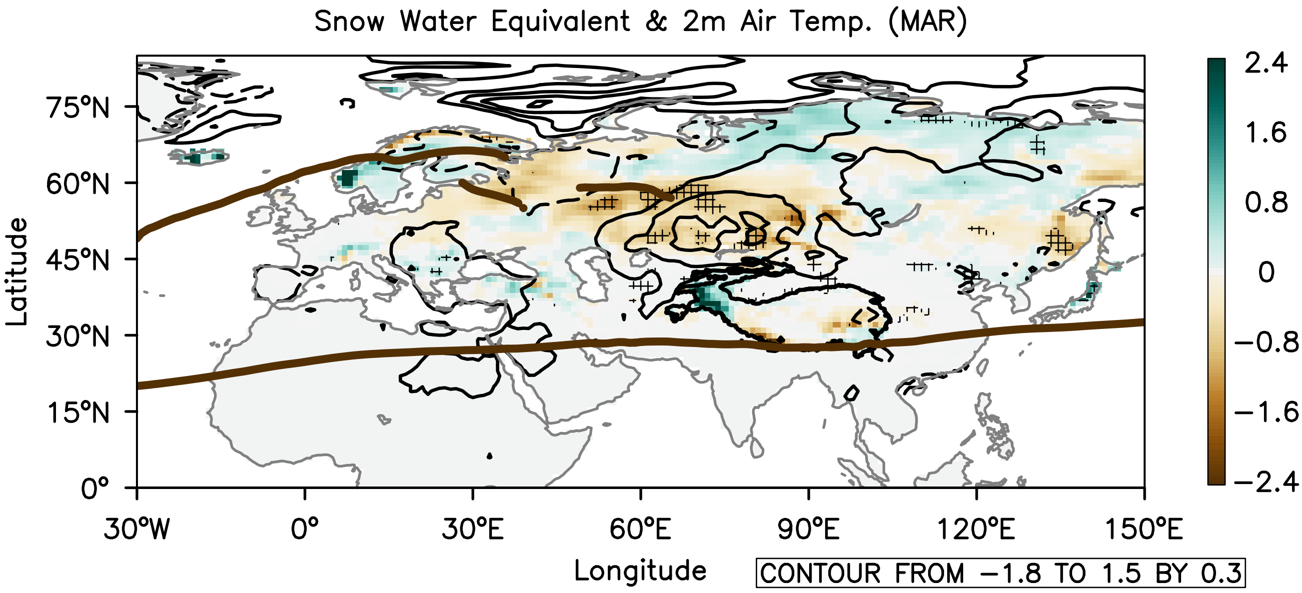

Snow Water Equivalent & 2m Air Temp. (MAR)
75°N
60°N
45°N
30°N
15°N
0°
Latitude
30°W
0°
30°E
60°E
90°E
120°E
150°E
Longitude
CONTOUR FROM −1.8 TO 1.5 BY 0.3
2.4
1.6
0.8
0
−0.8
−1.6
−2.4

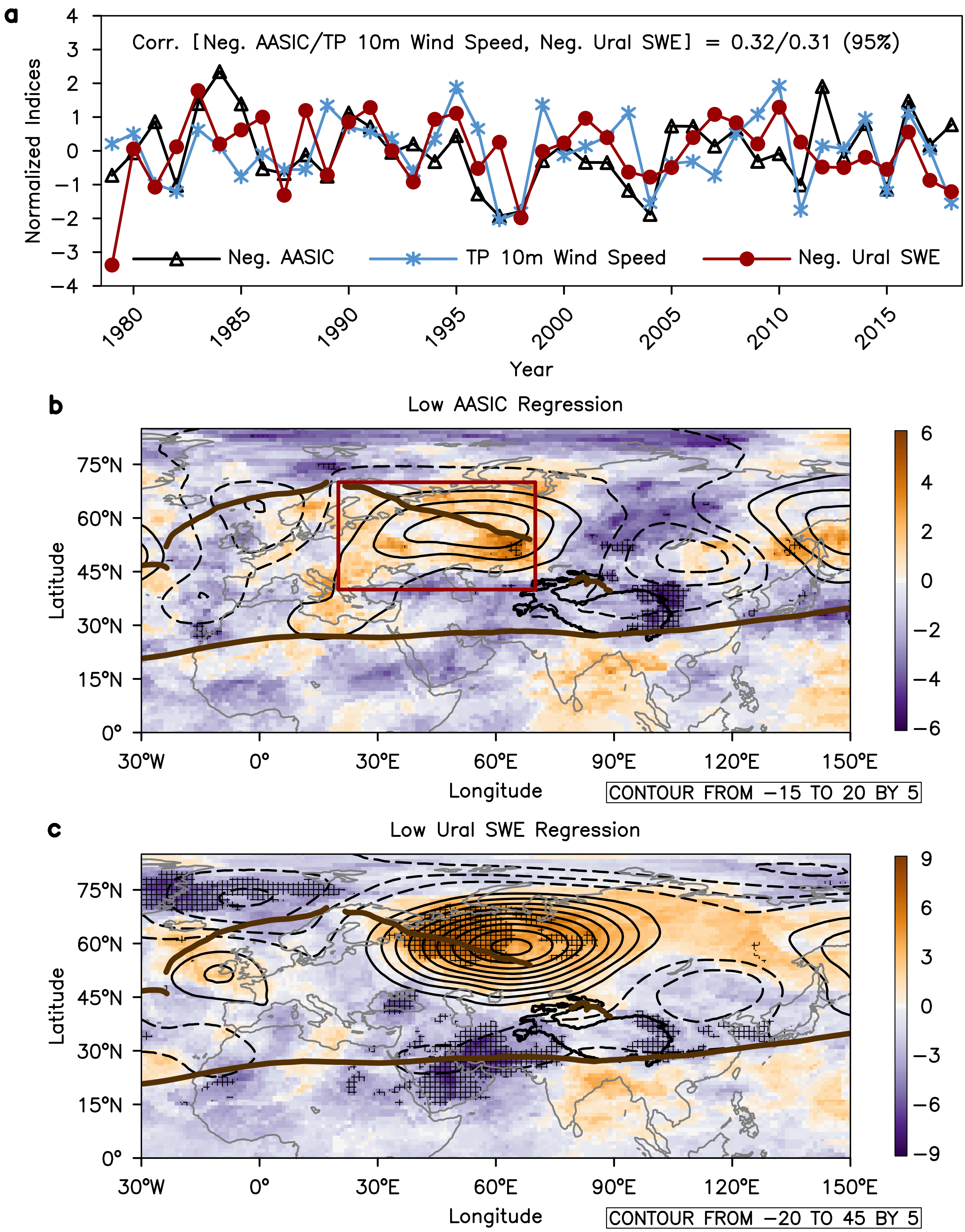

This document is the Accepted Manuscript version of a Published Work that appeared in final form in Nature Climate Change, after peer review and technical editing by the publisher.
To access the final edited and published work see https://doi.org/10.1038/s41558-020-0881-2

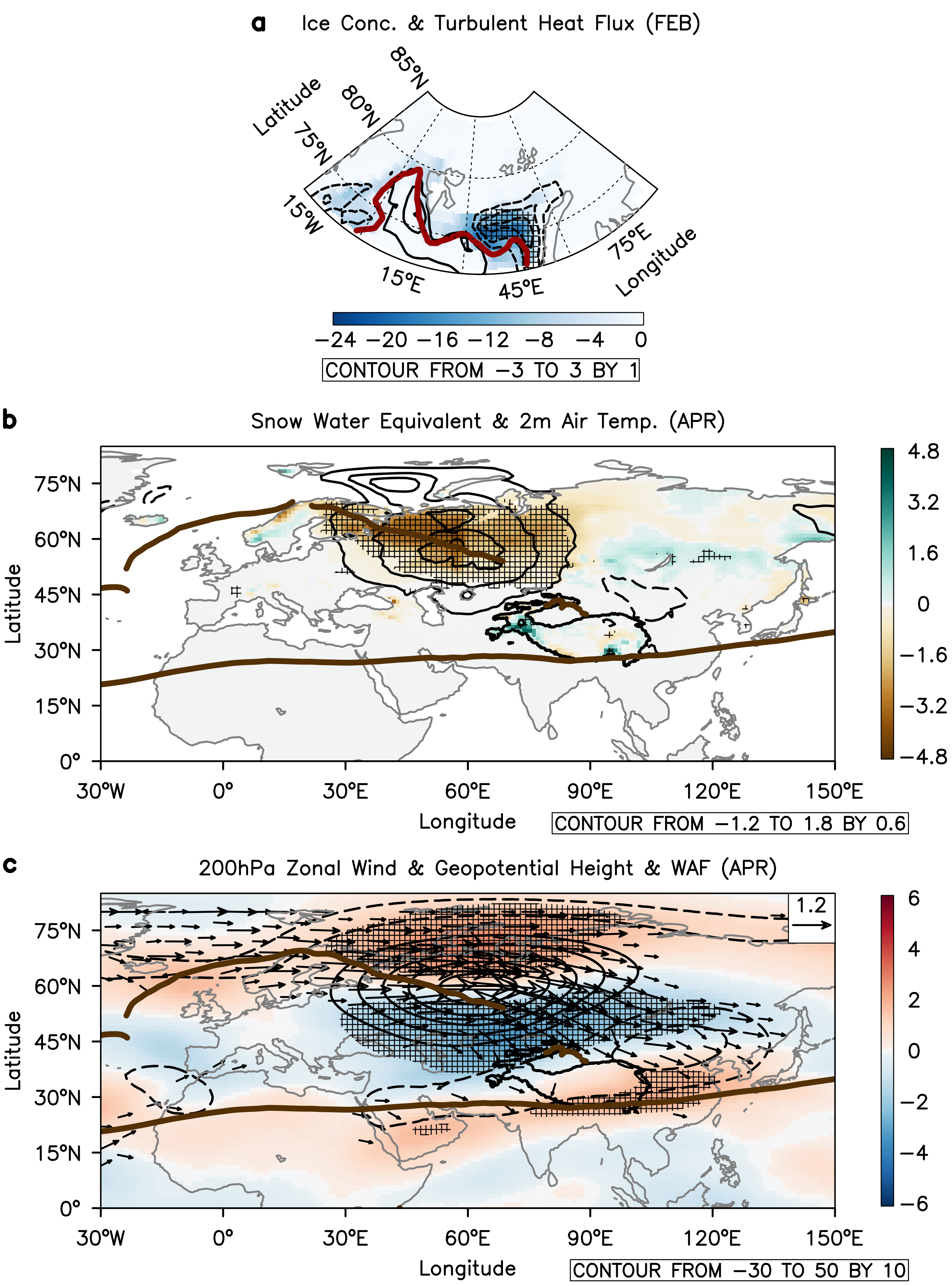
a
Ice Conc. & Turbulent Heat Flux (FEB)
85°N
80°N
75°N
Latitude
15°W
15°E
45°E
75°E
Longitude
−24 −20 −16 −12 −8 −4 0
CONTOUR FROM −3 TO 3 BY 1
b
Snow Water Equivalent & 2m Air Temp. (APR)
75°N
60°N
45°N
30°N
15°N
0°
Latitude
30°W 0° 30°E 60°E 90°E 120°E 150°E
Longitude
4.8
3.2
1.6
0
−1.6
−3.2
−4.8
CONTOUR FROM −1.2 TO 1.8 BY 0.6
c
200hPa Zonal Wind & Geopotential Height & WAF (APR)
1.2
75°N
60°N
45°N
30°N
15°N
0°
Latitude
30°W 0° 30°E 60°E 90°E 120°E 150°E
Longitude
6
4
2
0
−2
−4
−6
CONTOUR FROM −30 TO 50 BY 10

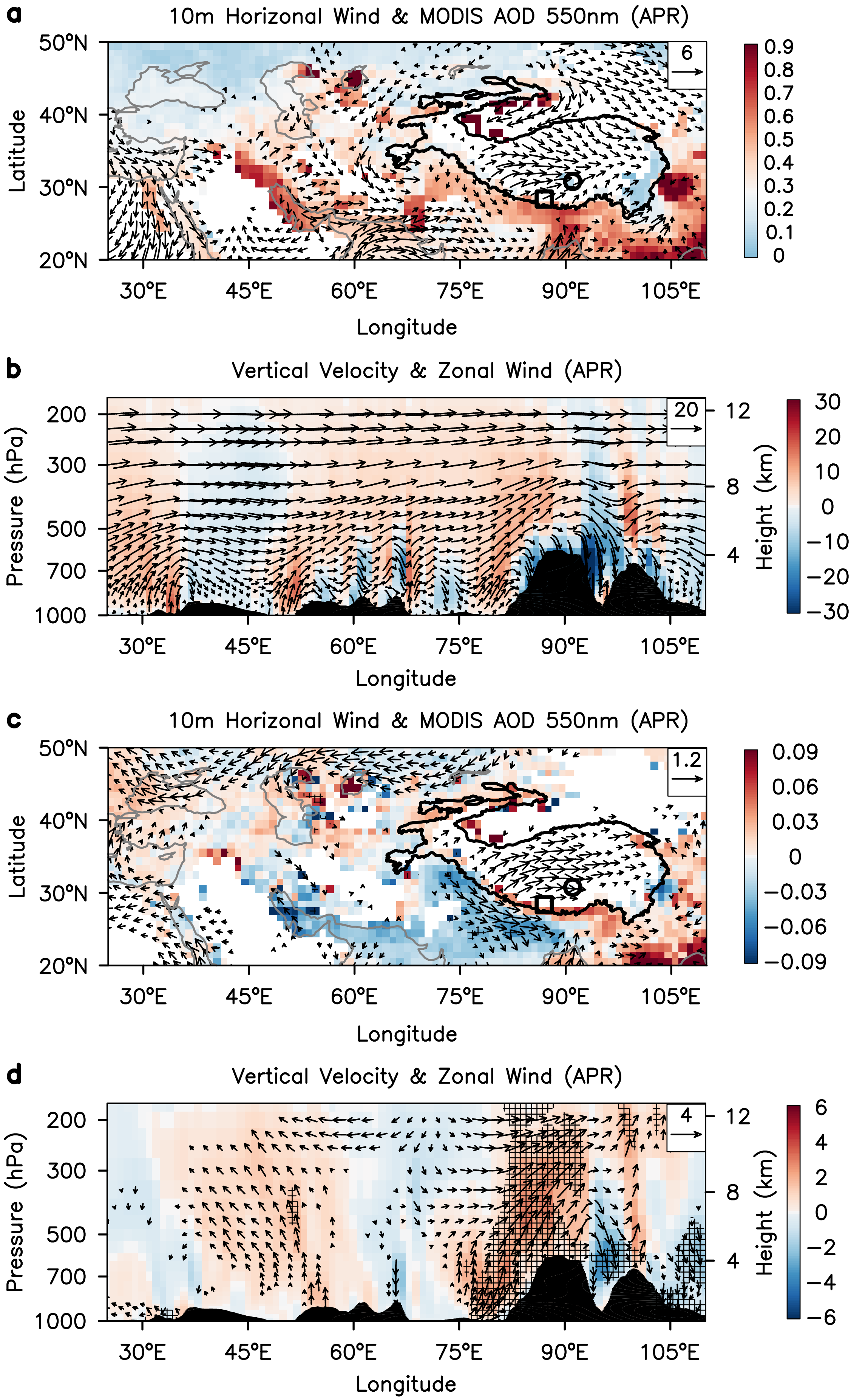

a
10m Horizontal Wind & MODIS AOD 550nm (APR)
b
Vertical Velocity & Zonal Wind (APR)
c
10m Horizontal Wind & MODIS AOD 550nm (APR)
d
Vertical Velocity & Zonal Wind (APR)
Latitude
Longitude
Pressure (hPa)
Height (km)
50°N
40°N
30°N
20°N
30°E
45°E
60°E
75°E
90°E
105°E
200
300
500
700
1000
12
8
4
6
20
1.2
4
0.9
0.8
0.7
0.6
0.5
0.4
0.3
0.2
0.1
0
30
20
10
−10
−20
−30
0.09
0.06
0.03
−0.03
−0.06
−0.09
6
2
−2
−4
−6

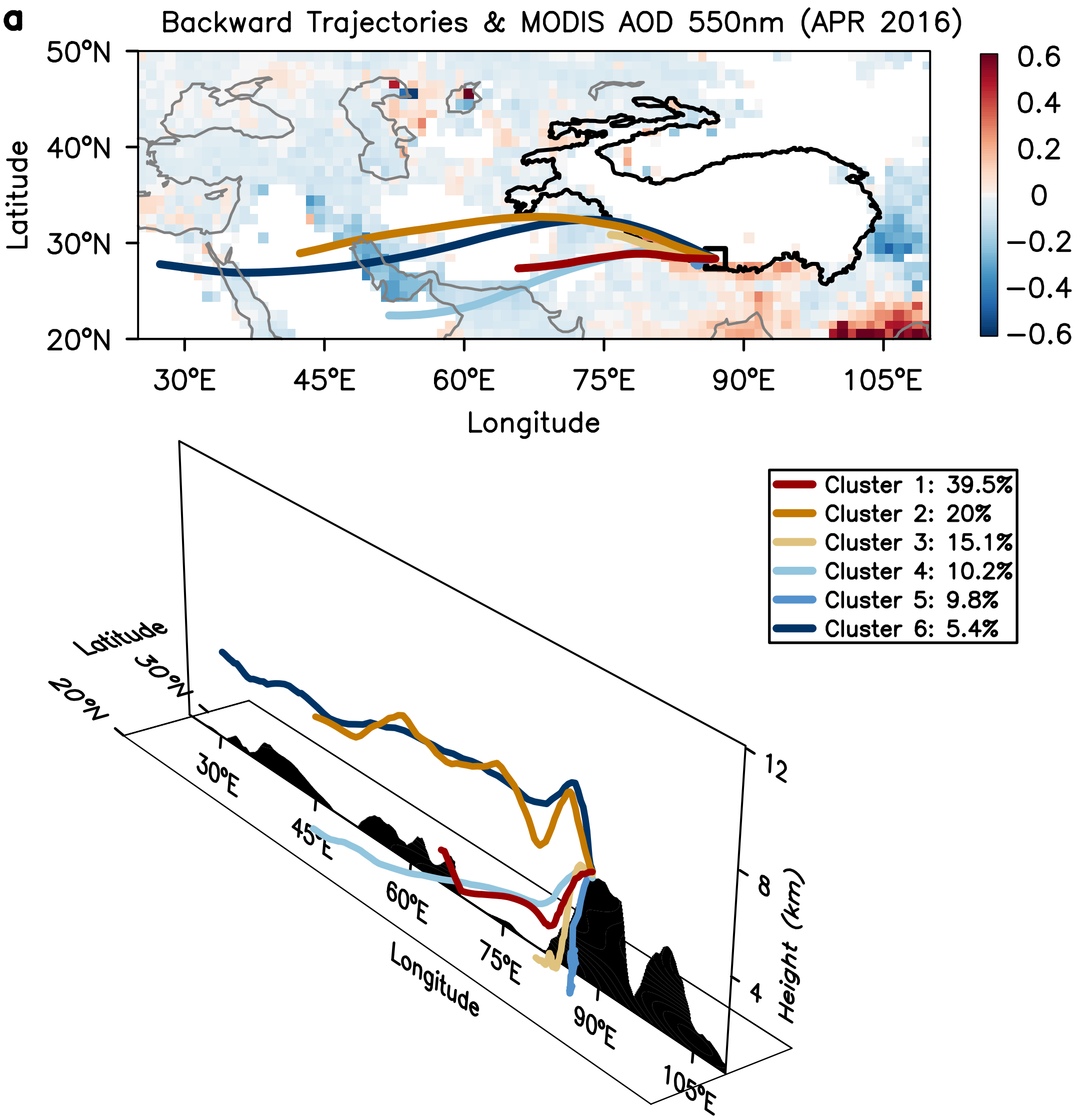
a
Backward Trajectories & MODIS AOD 550nm (APR 2016)
Latitude
Longitude
Cluster 1: 39.5%
Cluster 2: 20%
Cluster 3: 15.1%
Cluster 4: 10.2%
Cluster 5: 9.8%
Cluster 6: 5.4%
Height (km)

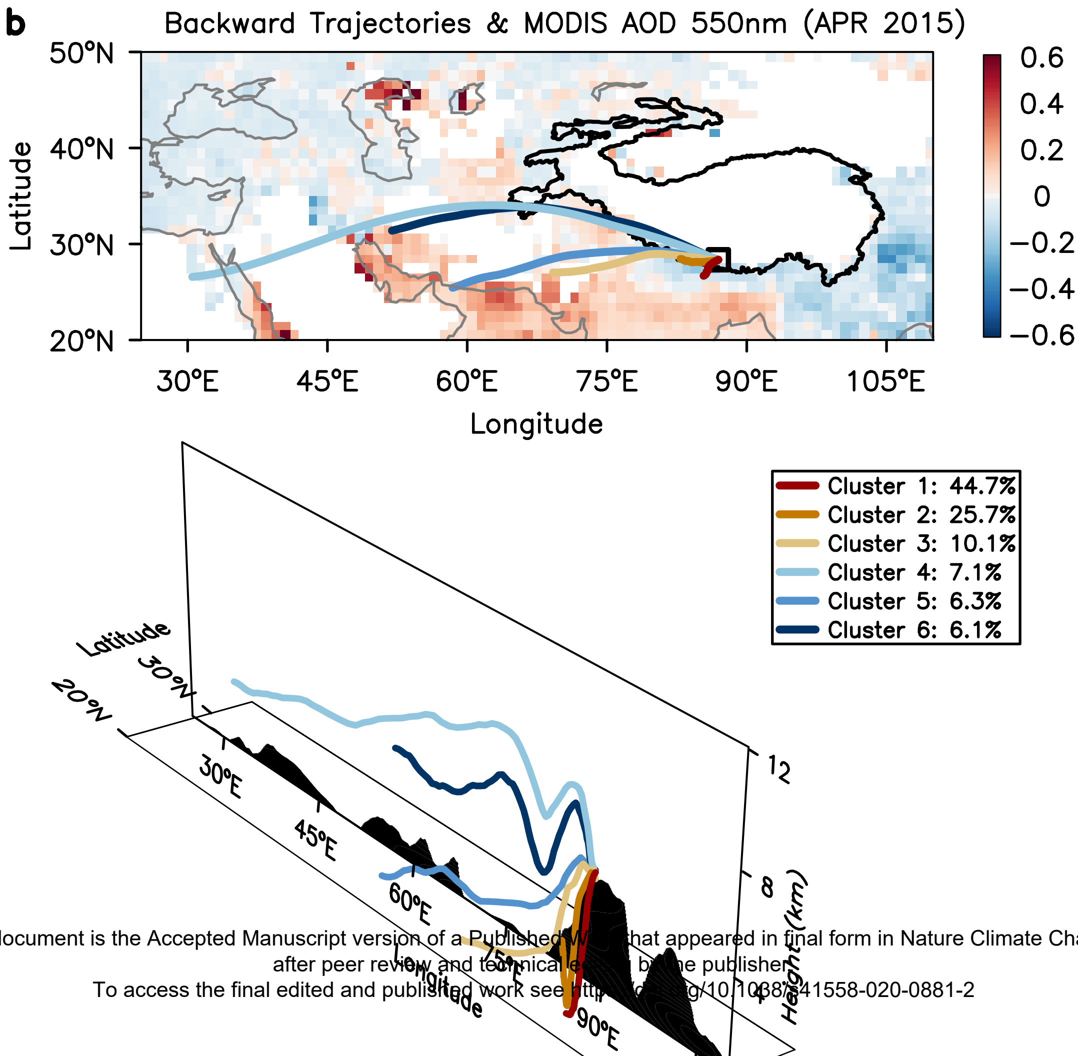
b
Backward Trajectories & MODIS AOD 550nm (APR 2015)
Latitude
Longitude
Cluster 1: 44.7%
Cluster 2: 25.7%
Cluster 3: 10.1%
Cluster 4: 7.1%
Cluster 5: 6.3%
Cluster 6: 6.1%
Height (km)